Laboratory Observations of Foam Generation from Field-Scale Breaking Waves

Lily Nguyen

A thesis
submitted in partial fulfillment of the
requirements for the degree of

Master of Science

University of Washington

2024

Committee:
C. Chris Chickadel
Christopher Bassett

Program Authorized to Offer Degree:
Civil and Environmental Engineering

University of Washington

Abstract

Laboratory Observations of Foam Generation from Field-Scale Breaking Waves

Lily Nguyen

Co-Chairs of the Supervisory Committee:
C. Chris Chickadel
Department of Civil & Environmental Engineering

Christopher Bassett
Department of Mechanical Engineering

Wave generated bubbles are a primary mechanism for air-sea flux of heat, gas, and momentum, aerosol production, ambient noise generation, and energy dissipation due to breaking in the open ocean. An actively breaking wave, or whitecap, entrains air, leaving behind a bubbly wake. Bubbles rise to the air-sea interface, and residual foam develops from the receding wake. Previous small-scale laboratory research by Masnadi et al. (2021) has shown that under conditions of outward heat flux from the ocean to the atmosphere, the thermal time scale of cooling surface foam from wave breaking is related to bubble plume time scales and energy dissipation. This project involves further investigation of the thermal signature of cooling residual foam and its relationship to bubble formation and wave energy dissipation. To extend the hypothesis from Masnadi et al. (2021), an experiment with field-scale waves was conducted at the O.H. Hinsdale Wave Research Laboratory's Large Wave Flume at Oregon State University (OSU). In the experiment, one-meter plunging breakers were created from a solitary wave propagating over an individual shoal to initiate depth-limited breaking. Surfactant (Triton X-100) was added to the flume's freshwater to simulate the effects of saltwater on bubble formation and longevity of surface foam. In contrast to the conditions tested by Masnadi et al. (2021), inward heat flux conditions that generated a warm skin

were measured at OSU. At different locations along the wave flume, a combination of optical and thermal remote sensing, acoustic, and in-situ instruments were used to measure and map horizontal variability of bubble plume geometry, bubble size distribution, and whitecap foam coverage. The analysis focuses on time scales associated with visible foam, subsurface bubble plumes, onset times from breaking to warming of residual foam, and estimates of the energy dissipation rate, and the results show both similarities and differences to those found previously.

TABLE OF CONTENTS

LIST OF FIGURES

LIST OF TABLES

ACKNOWLEDGMENTS

Thank you to my advisors, Chris Chickadel and Chris Bassett, for all your guidance, compassion, and encouragement over the last few years. It has been one of the greatest pleasures to be mentored by insightful scientists and engineers. This work is one of the proudest moments in my life, and I am happy to share this work with you. I would also like to thank my amazing parents, sister, and brother who have supported me up until this point. They inspire me to grow as an academic and person.

To all the friends that I have made in Seattle and California, thank you for keeping me grounded through the tough times and lifting me in times of need. I could not have asked for a better support system. Thanks to my best friend Michelle Tanaka, without you, I would not have studied engineering and gone down this path. For your camaraderie from my peers at the Environmental Fluid Mechanics group, thank you for the shared memories from our lunches, happy hours, impromptu office talks, and the retreat. It has been wonderful to be part of this welcoming community.

This research was made possible by funding from the National Science Foundation. This work was conducted at the Natural Hazards Engineering Research Infrastructure Hinsdale Wave Research Laboratory at Oregon State University. Thank you for the Washington NASA Space Grant Fellowship program for additional support. Finally, thank you to the Civil and Environmental Engineering Department at UW and the Air-Sea Interactions and Remote Sensing Department at APL for academic resources and support.

Chapter 1

INTRODUCTION AND MOTIVATION

1.1 Waves and Linear Wave Theory

Waves are basic physical phenomena in which information can be relayed between two points in space and time [1]. Wave motion occurs when a disturbance is acted onto a medium at a stable equilibrium state, carrying energy, and a restoring force returns the medium back to equilibrium. In fluid dynamics, waves are generalized into four types: sound, gravity, capillary, and planetary. Sound waves are due to the compressibility or elasticity of the fluid medium. Gravity waves exist in which gravity is the restoring force, and a subset of gravity waves are internal gravity waves that exist at the interface between two fluids of different densities. At the phase boundary of a fluid, capillary waves can propagate and create ripples due to surface tension. Lastly, planetary or Rossby waves are induced by planetary rotation, and the restoring force is the inertial Coriolis force.

Under linear wave theory, also known as Airy wave theory and small-amplitude wave theory [2], gravity waves are described to propagate on the surface of a homogeneous fluid layer. The wave equation

$$\frac{\partial^2 \eta}{\partial t^2} = c^2 \nabla^2 \eta, \tag{1.1}$$

is a second-order linear partial differential equation that describes water wave motion propagating in the x-direction, where η is any disturbance, The general unchanging form of the wave equation is

$$\eta = f(x - ct) + g(x + ct), \tag{1.2}$$

where f and g are arbitrary functions and c is a non-negative real coefficient. Under Fourier's Principle, any arbitrary disturbance can be decomposed into sinusoidal wave components in

the form

$$\eta = a \sin\left[\frac{2\pi}{L}(x - ct)\right]. \tag{1.3}$$

This sinusoidal form can be used to distinguish properties of the wave. The $2\pi(x - ct)/L$ is the phase of the wave. The amplitude of the wave is determined by a. Wave height H is twice the wave amplitude $2a$, describing the elevation difference between crest and trough. Wavelength is described as L. A commonly used parameter is wavenumber k which is defined as

$$k \equiv \frac{2\pi}{L}. \tag{1.4}$$

Wavenumber is the number of complete waves in the length 2π. Another important characteristic of a wave is the period T, which is defined as

$$T = \frac{L}{c}, \tag{1.5}$$

where c is the speed of propagation of the wave, or phase speed. Wave period can be used to find angular frequency:

$$\omega = \frac{2\pi}{T}. \tag{1.6}$$

Small amplitude waves propagate with the velocity c. Individual water particles move in orbital motion. In deep water ($d/L > 1/2$, where d is the depth), particle orbits are circular. In shallow water ($d/L < 1/20$), the particle orbits are elliptical. The orbital size decreases with depth. In shallow water, water particle oscillatory motion extends over the entire water column, and in deep water, the wave motion does not extend down to the bed (Figure 1.1). For transitional water depth ($1/20 < d/L < 1/2$), the dispersion relations are used to describe wave motion. The dispersion equation is

$$\omega = \sqrt{gk \tanh kH}, \tag{1.7}$$

where H is wave height and g is gravitational acceleration. Dispersion explains wave motion as waves with different wavelengths move at different phase speeds. Phase speed is given by

$$c = \sqrt{\frac{gL}{2\pi} \tanh \frac{2\pi H}{L}}. \tag{1.8}$$

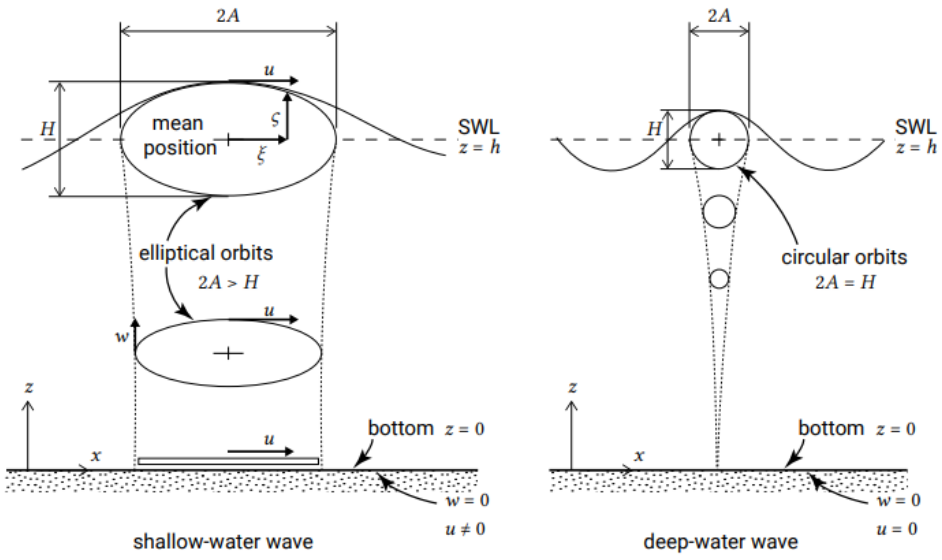

Figure 1.1: Orbital motion under linear wave theory for shallow and deep water conditions, from Bosboom's *Coastal Dynamics* [3].

As the dispersion relation is implicitly related to the wavenumber k, phase speed can be simplified based on the relation between water depth d and wavelength L. The deep water approximation describes phase speed as

$$c = \sqrt{\frac{gL}{2\pi}} = \sqrt{\frac{g}{k}}. \tag{1.9}$$

The shallow water approximation describes phase speed as

$$c = \sqrt{gH}. \tag{1.10}$$

1.2 Non-Linear Waves, Wave Breaking and Energy Dissipation

Complexities in waves can create asymmetric and skewed characteristics and eventually, non-linearity. Wind can blow on a flat water surface, and distortions of the water surface create non-linearities. As a wave travels onshore and bathymetry steepens during shoaling, waves become non-linear and possibly break. These complexities are not captured by linear wave theory.

During nearshore shoaling, a wave propagates from deep water to intermediate and shallow water toward onshore. As this happens, wavelength decreases and wave height increases, causing the face of the wave to steepen and eventually break. McCowan (1894)[4] first described the relationship between water height H and water depth d with the breaker index:

$$\gamma = \frac{H}{d}. \tag{1.11}$$

According to solitary wave theory for shallow water, the process of breaking happens from the instability of the wave crest[5] and the breaker index γ_b is at least 0.78 [3]. Wave height, length, and direction of propagation are all impacted by bathymetry, transforming waves. Energy is lost through processes such as refraction shoaling, bottom friction, and wave breaking. The energy that is lost or gained in a system can be understood with the energy conservation equation [3]:

$$\frac{\partial E}{\partial t} + \frac{\partial}{\partial x}(Ec_g cos\theta) + \frac{\partial}{\partial y}(Ec_g sin\theta) = S - D. \tag{1.12}$$

The energy conservation equation is described as the sum of the change of energy and the import of energy in the x-direction and the y-direction is equivalent to the gain of energy, where wave energy density E is [3]

$$E = \frac{1}{8}\rho g H_{rms}^2, \tag{1.13}$$

where c_g is wave group speed, H_{rms} is the root mean square of wave height, θ is the wave direction concerning the x-axis or perpendicular to the coastlines, S is the energy generation, and D is energy dissipation.

The Iribarren parameter classifies waves into different breaker types: surging, collapsing, plunging, or spilling, shown in Figure: 1.2. It is described by

$$\xi = \frac{\tan\alpha}{\sqrt{H_0/L_0}}, \tag{1.14}$$

where $\tan\alpha$ is the steepness of the beach[3], H_0 is the wave height in deep water and L_0 is the wavelength in deep water. When $\xi > 5$ and shores are steep relatively to long swell waves,

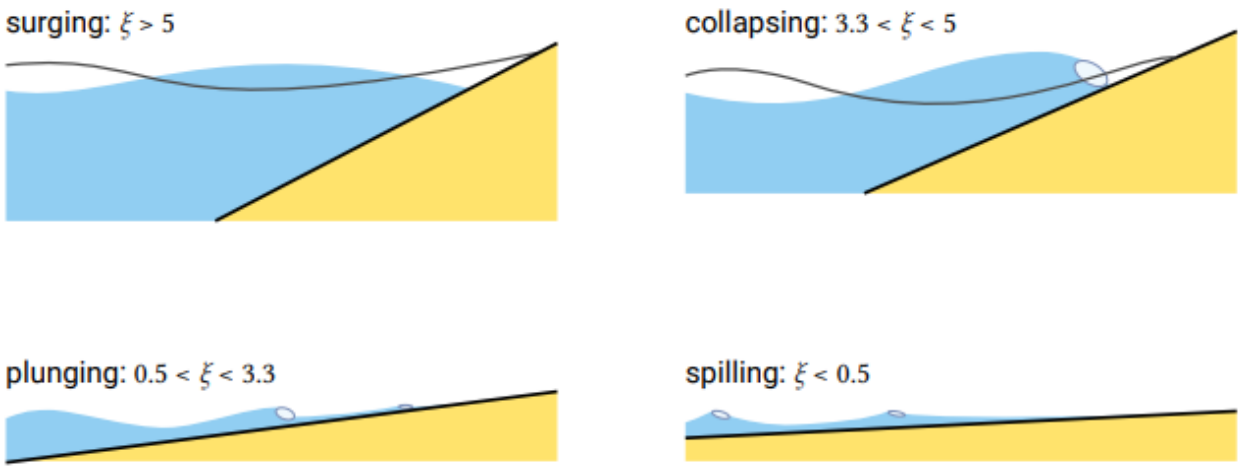

Figure 1.2: Breaker types. Images from Bosboom's *Coastal Dynamics*[3].

the breaking is surging; waves surge vertically with little air entrainment, or whitewater. Plunging waves ($0.5 < \xi < 5$), correspond to waves whose crests curl over the trough. When $3.3 < \xi < 5$, the breaking is collapsing. Collapsing waves are between surging and plunging waves. Spilling breakers ($\xi < 0.5$) are characterized by the crest of the wave gradually toppling down the face of the wave. These are commonly observed under breaking wave conditions in the open ocean or areas with relatively gradual changes in cross-shore bathymetry. As a breaking wave generates a mixture of air and water layer in the upper water column, a surface roller serves as a storage of energy and momentum before dissipating through turbulence[3]. In addition, air is injected into the water column, generating a bubble beneath the surface and whitecap foam. As the bubbles reach the surface, they burst, releasing spray droplets and marine aerosol.

Wave breaking in the open ocean is driven by the input of energy from the wind[6]. At low wind speeds, short waves do not entrain enough air to generate bubbles. At moderate and high wind speeds, bubbles are generated by wave breaking, which is the primary mechanism for air-sea flux of heat, gas, and momentum, aerosol production, ambient noise generation, and energy dissipation.

The understanding of water wave mechanics and its associated processes is significant to society because the ocean and coasts are utilized for economic, political, and social purposes. Approximately 40% of Americans live near the coasts. Coastal areas produce $9.5 trillion in goods and services and employ 58.3 million people[7]. Scientists study oceanic and coastal processes to further understand these processes and create models and forecast predictions.

1.3 Bubble Plumes and Whitecap

The term "whitecap" is typically used to describe active foam generated by a breaking wave crest or the passive residual foam following the crest [8]. The injected air by wave breaking creates a bubble plume. The active breaking process is complete when no further air is entrained. Active foam is referred to as "acoustically active" and describes when bubbles generated by breaking create underwater sound [9]. The passive process describes the evolution of the bubble plume as it decays into residual foam [10, 8]. The distribution of bubble sizes present in the water column evolves due to dissolution, buoyant-driven transport, and bubble coalescence. Publications report bubble size distributions under breaking waves that are dependent on the stage of breaking (i.e., active/passive) and size of the bubble [11, 12, 13, 14, 15, 9]. The Hinze scale describes a representative maximum bubble size and corresponds to the threshold at which the largest bubbles are not fragmented by turbulent sheering. A representative Hinze scale is on the order of 1 mm. Although rise velocities versus bubble size relationships are not linear, larger bubbles have faster rise velocity[16] and have a greater significant impact on the void fraction, or fraction of total gas volume to the total volume of a sample [17]. Large bubbles (e.g., $a > 1$ mm) contribute significantly to active whitecaps and passive residual foam [18]. In literature, actively breaking is commonly referred to as Stage A whereas Stage B refers to the subsequent passive process [9]. The term whitecap coverage W describes the percentage area that is visually covered by foam. W_A is described as whitecap coverage associated with breaking rate and energy dissipation[10], and W_B is associated with marine aerosol production[19, 20]. Previous measurements of whitecap coverage were taken through laborious visible imagery[21]. Callaghan and White

(2009)[22], developed techniques to automate the processing of high-resolution digital imagery to quantify W. However, further work is necessary to objectively distinguish Stage A and Stage B using Callaghan and White's method. Anguelova and Webster (2006)[23] observed whitecap coverage and wind speed have a scattered relationship over three orders of magnitude, proposing other factors that need to be considered. In Callaghan et al. (2008) and Callaghan et al. (2012)[24, 25], they inferred that environmental factors such as wave field characteristics, breaker type, surfactants, and differences in image processing techniques can affect the observed relationship. Among other observations, they note that the surfactants and breaker type caused variations in bubble and foam stability and bubble plume characteristics.

Callaghan et al. (2013) [19] conducted laboratory experiments to measure visible decay times for foam (τ_{foam}) and bubble plumes (τ_{plume}). Whitecap decay describes a Stage B whitecap and can be visually observed and measured at the water surface. Callaghan (2012) [25] speculated surfactants play a significant role in the whitecap foam decay time. Variations in foam decay times can be contributed by the complex bubble and surfactant interface interactions, surfactant chemisty and variability in bubble plume characteristics. They suggested that the lower limit of foam lifetime is correlated with the lifetime of bubble plumes, which is supported by Monahan and O'Muircheartaigh (1986) [20]. Generally, Stage B occupies more whitecap coverage than Stage A due to the resupplying of dispersed surfacing bubbles. The ratio of Stage B to Stage A whitecap coverage ranges from 1.5 to 40 [26, 8, 10]. Phillips (1985)[27] related whitecap coverage to average bubble persistence and wave breaking rate according to

$$W = \int_0^\infty \tau_{bub} c L(c) dc, \tag{1.15}$$

where τ_{bub} is the bubble persistence time, $L(c)$ is the Phillips parameter and c is the forward speed of the breaking wave crest. The Phillips parameter describes the wave-breaking characteristics and is dependent on wave speed.

There is a large variability in the decay time of whitecap foam due to the effects of surfactants, which affect the foam stability and bubble plume characteristics. These factors

are also impacted by the wave-breaking dynamics[25]. Based on measurements of the effects of surfactants on whitecap foam decay time, Callaghan et al. (2013) [19] concluded that τ_{plume} is proportional to the energy dissipation [19]. Comparing trials without surfactants, the foam decay time is related to the bubble decay time. With surfactants, the plume decay time can be scaled from the time to the onset of cooling foam t_{cool} [28].

Using clean water and water with a surfactant (Triton-X at 204 $\mu g L^{-1}$) under different wave packets, Masnadi et al. (2021) (MCJ2021) [28] observed τ_{plume} is proportional to the increase in energy dissipation for different breaker types from spilling to plunging. The presence of surfactant affected the scaling between τ_{plume} and τ_{foam} because surfactants stabilize bubbles. Therefore, bubbles will reside at the surface for longer periods. They did note that the relationship between τ_{plume} and maximum foam area is caused by the wave-breaking dynamics that control plume characteristics. However, there was no investigation of the plume characteristics and how they change over time.

1.4 Thermodynamics

At the surface of the ocean, heat is transferred through four main processes: shortwave radiation Q_s is absorbed by the ocean water from the sun on the infrared spectrum, radiative heat Q_b is exchanged between the atmosphere and the ocean, latent heat Q_e is lost from the ocean during evaporation, and sensible heat Q_h is exchanged at the air-sea interface [5]. The overall oceanic heat flux (kcal cm^{-2} yr^{-1}) balance Q_T is described by

$$Q_T = Q_s - Q_b - Q_e - Q_h. \tag{1.16}$$

The energy Q_s that the ocean receives from the sun is primarily in the visual spectrum (400 to 700 nm) and infrared ranges (750 nm to 1000 μm), and less than 10% percent of the energy is ultraviolet (300–400 nm). Due to the earth's atmosphere, most of the ultraviolet and infrared energy is absorbed or scattered before it reaches the ocean surface. Rayleigh scattering gives the sky and ocean blue color due to selective scattering of shorter wavelengths. Blue light is on the shorter end of the visible spectrum and is less absorbed and penetrates deeper into

the water column than other wavelengths [5].

All bodies with a nonzero absolute temperature radiate energy to their surroundings. This is described by the Stefan-Boltzmann law,

$$Q_b = \sigma T^4, \tag{1.17}$$

where σ is the constant of proportionality or the Stefan–Boltzmann constant and T is the absolute temperature of a body. The Stefan-Boltzmann Law of radiation calculates the effective black body radiation Q_b [5]. In practice, the heat flux associated with related to black body radiation is dependent on the surroundings and emissivity of the object (1 for an ideal radiator) such that total radiation heat exchange environment's humidity and temperature. Stefan-Boltzmann law can be rewritten as

$$Q_b = \sigma e(T^4 - T_C^4), \tag{1.18}$$

where e is the emissivity and T_C is the surrounding temperature assuming it is cooler (e.g., the sky relative to the ocean's surface).

Latent heat of evaporation Q_e is heat loss due to the phase change from evaporation [5]. It is typically the largest heat term in Eq. 1.16[5] and it is enhanced by breaking waves, wind, and sea spray. This heat term is a bulk approximation determined by

$$Q_e = C(e_w - e_a)W, \tag{1.19}$$

where e_w is the vapor pressure at the ocean's surface, e_a is the vapor pressure in the air above the ocean's surface, C is a numerical constant, and W is wind speed.

Sensible heat loss Q_h[5] is heat lost due to conduction and convection from the temperature difference at the ocean's surface and the air above it. Sensible heat is estimated to be on the order of 10-15 percent of the latent heat of evaporation[5].

The impacts of wave breaking, bubble, and surface foam on heat transfers at the air-sea interface have been the focus of a wide range of studies in laboratory and field environments. At a whitecapped ocean surface, the air and water near the surface are multi-phase with the

air containing droplets and the bubbles present in relatively high densities in the water. This multi-phase air-sea interaction increases the effect surface area [29] and possibly enhances heat transfer[30]. Past studies investigating the interstitial exchange at thin bubble walls suggest that cooling at the air-sea interface can be enhanced by the relatively small thermal mass of foam to the bulk water[31]. In contrast, Andreas et al. (2000) [32] investigated the latent and sensible heat fluxes of bubbles from wave breaking suggesting that bubbles are not a significant factor in the cooling of the water surface. However, Jeong et al. (2012) [33] suggested that spray increases enthalpy transfer through evaporation. In Chickadel et al. (2022) [34], direct heat flux measurements of sea foam were conducted and their results confirmed that foam-covered surfaces enhanced heat flux relative to foam-free surfaces. Warm bulk water is brought toward the surface by bubbles. Once the bubbles reach the surface, they thin and burst. During this process, the air inside the bubble is warmed through sensible heat flux and the surrounding fluid cools due to latent and sensible heat fluxes into the bubble. This is attributed to differences in the sensible and latent heat fluxes as bubbles create an unstable boundary layer at the surface, inferring enhanced cooling.

The observation that enhanced cooling is generally observed for foam suggests that remote sampling methods focused on thermal sensing could be a valuable tool for studying breaking waves. Jessup et al. (1997) first clearly showed bright active whitecap in infrared imagery, suggesting that the bright whitecap contrast with the darker residual shows a difference in temperature due to emissivity [35]. This created a new potential method to estimate the infrared emissivity of active foam and sea surface temperature using remote sensing. Marmorino and Smith (2005) [36] report the rapid cooling of foam following a passing wake, using infrared imagery, and discovered the ability to differentiate between active and residual stages of whitecap foam. Chickadel et al.(2022) [34] reported cooling is caused by enhanced evaporation from bubbles and the process of cooling initiates after the bubbles stop rising and reach the surface, after foam generation. An example of the thermal imagery demonstrating the ability to detect the cooling of foam is shown in Figure 1.3.

Further work studying the thermal signals associated with breaking waves was performed

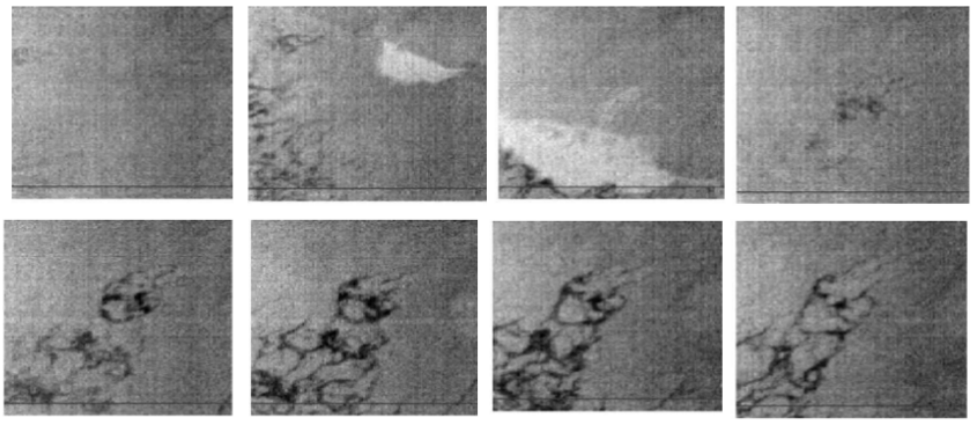

Figure 1.3: Examples of infrared imagery sequence of a breaking wave in the surfzone, showing cooling residual foam in the wave's wake, from unpublished data taken by A. Jessup (personal communication). These image panels progress from the upper left panel down to the lower right. Lighter shades of gray are warmer and darker shades are colder temperatures.

by MCJ2021. In a laboratory setting (the tank is 12 m long, 0.91 m wide, and 1.2 m tall), they observed a direct relationship between the time scales of bubble plumes and surface foam to the energy dissipated by breaking waves. The beginning of cooling of the foam, t_{cool}, was used to quantify the total plume decay time τ_{plume} and maximum plume depth d_{max}. The time scale t_{cool} is defined as the time from when breaking starts to the time when foam temperature starts to cool (Figure 1.4). Using t_{cool} and d_{max}, it can infer plume characteristics and the associated energy dissipation based on surface temperature measurements. The presence of surfactants should not significantly affect the bubble plume evolution[28]; large bubbles (larger than 1 mm) are less likely to be affected by surfactants. However, small bubble formation and their size distributions and foam generation will be affected by surfactants[19].

These prior results motivated a study to investigate the time from breaking and the initiation of cooling from foam and its relation to the time during foam generation due to rising bubbles and bubble plume decay. The goal of this Foam Experiment (FoamEX) project is to confirm (1) the onset of cooling of residual foam from a wake following a

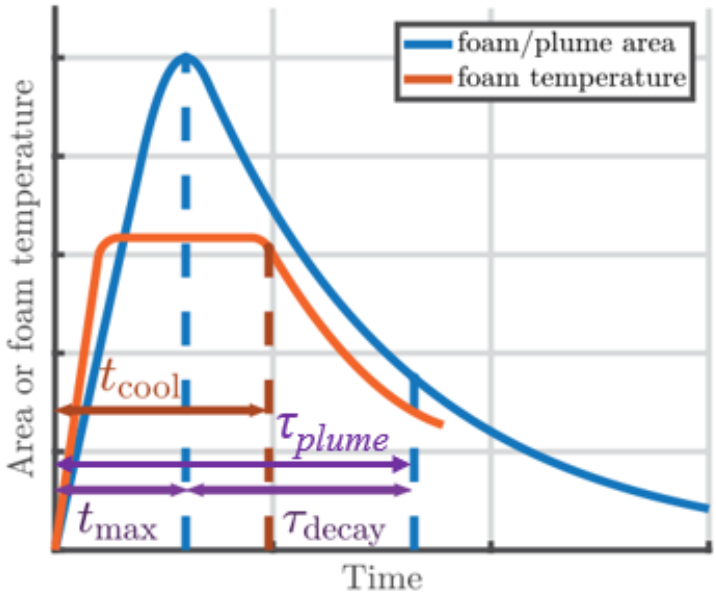

Figure 1.4: A conceptual model, modified from MCJ2021, of the relationship between foam or bubble plume area (blue) and foam temperature (orange) showing relevant time variables: t_{cool}, the time from the initial breaking (t=0) to the onset of foam cooling, t_{max} , the time t=0 to the maximum area, τ_{decay}, area decay time scale which is equal to the e-folding time of decay from the maximum area, and τ_{plume} where $\tau_{plume} = \tau_{decay} + t_{max}$.

breaking wave can be used to quantify bubble plume decay depth for field-scale waves, (2) the spatial variability of cooling foam can be used to map the spatial variability of bubble plume depth and bubble plume rise velocity, and (3) the correlation between bubble size and spatiotemporal plume evolution to wave energy flux through thermal signature.

Chapter 2

METHODS

2.1 Experimental setup

2.1.1 Oregon State University Hinsdale Wave Labortory

To further investigate the spatial variability of foam decay and its relation to the spatial variability of bubble plume evolution, we conducted an experiment at the O.H. Hinsdale Wave Research Laboratory (HWRL) at Oregon State University from August 8-12, 2022. The Large Wave Flume (LWF) at HWRL is 104 m long, 3.7 m wide, and 4.6 m high (Fig. 2.2), making it one of the largest wave flumes in North America. The internal length of the bottom of the flume is 87.42 m, and the beach has a 1:12 slope. A right-handed coordinate system is defined with the positive x-direction toward the beach (onshore). Positive z-direction is defined as vertically above the base of the tank. The origin is at the bottom center of the wavemaker. The wave type, water depth, and bathymetry can be adjusted to address the objectives of a given study.

The flume was filled with fresh water to a water depth of 2 m, adding ADV seed and 650 mL of Triton X-100 (resulting concentration of 1083.6 $\mu g/L$). To resolve patterns from individual wave-breaking events, solitary waves with a wave height of 1 m were generated. Under conditions with a flat bottom, the solitary wave would not break until arriving at the beach, so to initiate depth-limited breaking offshore, a bar was constructed. The bar spanned the width of the tank and, had an offshore portion of x = 17.7 to 39.7 (the bar had a 1:10 slope from x = 17.7 to 25.0 m), and was 17.7 m long, which resulted in breaking at approximately x = 39.7 m. From the breaking point to the start of the beach (x = 54.3 m), we collected measurements in six locations over a 12-m long section. The bathymetry of the flume configuration, breaking point, and sampling locations are shown in Figure 2.2.

Figure 2.1: Image of the Large Wave Flume looking from onshore to offshore

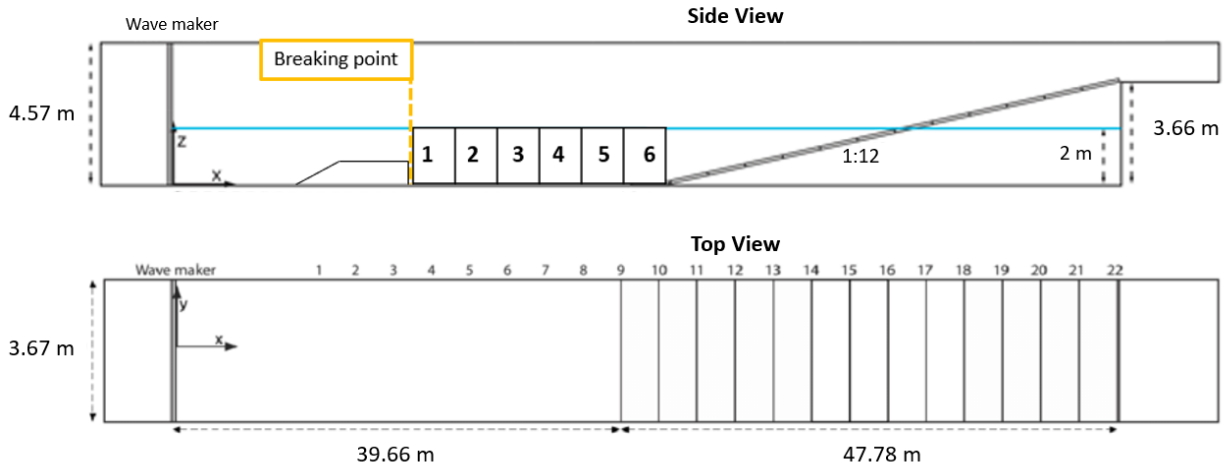

Figure 2.2: The top image is a side view of the LWF, showing the bathymetry of the experiment with a bar and six locations of measurements[37]. The bottom image is the top view of LWF.

On top of the walls of the wave flume, there was a cart system (shown in Fig. 2.3) that held our instruments. One cart was motorized to move along the x-axis of the flume (white cart) and could reposition the instrument cart (grey cart), which was 12 feet and had a mechanical traverse system to raise and lower the instruments (shown in Figs. 2.3 and 2.4) along the z-axis. Positioning of the instruments was achieved by attaching the carts and moving them to the desired location along the tank. Once in place, wooden stoppers were placed under the wheels to prevent the instrument cart from moving during sampling. Attached to the front of the instrument cart is a vertical frame where we mounted instrumentation looking down into the flume: two infrared cameras, a radiometer, and two visual cameras. Four instrument rails with hydrodynamic fairings were attached to the vertical traverse. The farings' shape reduces additional turbulence downstream. Echosounders, the acoustic velocity and attenuation system, acoustic doppler velocimeters (ADVs), void probes, temperature probes, and a bubble camera and light source system were attached to these faired rails to place them into the water. A schematic of above-water and below-water instrumentation

Figure 2.3: Image of the two carts on top of the walls of the flume. They ride above the tank to allow for instruments to be deployed into the flume at different locations and depths. The white cart is motorized to move along the tank. The instrument cart (behind the white cart in this view) is not motorized but can be pushed by the white cart to move along the tank. Two structures were mounted onto the instrument cart: one structure was used for top-view instruments, looking down into the flume and one structure was mounted onto fins to lower instruments into the water column.

Figure 2.4: Image of the front of our in-situ instruments. The instruments are attached to vertical farings that can be lowered or raised together. From the left structure (from top to bottom), the instruments are two void probes, one ADV, one void probe, and one ADV. The center structure, connected to two farings, has a light source and bubble camera in water housing units and the acoustic velocity and attenuation system. The faring on the right has upward-facing echosounders.

used in the study is shown in Figure 2.5.

2.1.2 Instrument and sensor array

Our approach to testing included a two-week experiment, which allowed time for setup, measurements, and breakdown. We specifically wanted to measure wave height profile H, wave energy dissipation, whitecap coverage W, void fraction, plume geometry metrics (plume area A_p, plume depth d_p, plume bubble size distribution $n(a)da$), and time scales (the lifetime of visible foam τ_{foam}, the lifetime of subsurface bubble plume τ_{plume}, and the time from start of breaking to the onset of residual foam temperature change $\tau_{cool/warm}$).

For surface foam and whitecap measurements, foam coverage area and foam temperature, we used two visual cameras (FLIR Blackfly, shown in Fig. 2.6) and two infrared cameras (DRS UC 17640, shown in Fig. 2.7). These cameras were mounted 4.7 m above the still water surface. The small-housing DRS (the right DRS camera in Fig. 2.3) had a 15-degree tilt (relative to the vertical), pointing to the right flume wall, The large-housing DRS (the left DRS camera in Fig. 2.3) had a 14-degree tilt, pointing to the left flume wall. Each infrared camera had a 40-degree field of view. DRS cameras sampled at a 30 Hz sampling rate (16-bit) with a 640x480 pixel array. Top-view Blackfly cameras had a 21-degree tilt. These two visual cameras have a wide view and a narrow view of the instruments. Lastly, a camera and a light system was deployed below the surface to image bubbles and determine bubble size near the surface where acoustics cannot resolve the bubble size. This system was utilized for the bubble shadowgraph technique, as used by Lichti and Bart (2018), where a third Blackfly camera with a telecentric lens was paired with a columnated light source, in underwater housings. Bubble camera images spanned approximately a 3 cm x 3 cm area with a resolution of 15 microns. The bubble camera system was located 20 cm below the water surface.

All Blackfly cameras had a sampling rate of 10 Hz and had a 2048x2448 pixel array. The top-view Blackfly cameras recorded 8-bit images while the subsurface Blackfly recorded 16-bit images. All cameras were recorded under one data acquisition system, using LabView

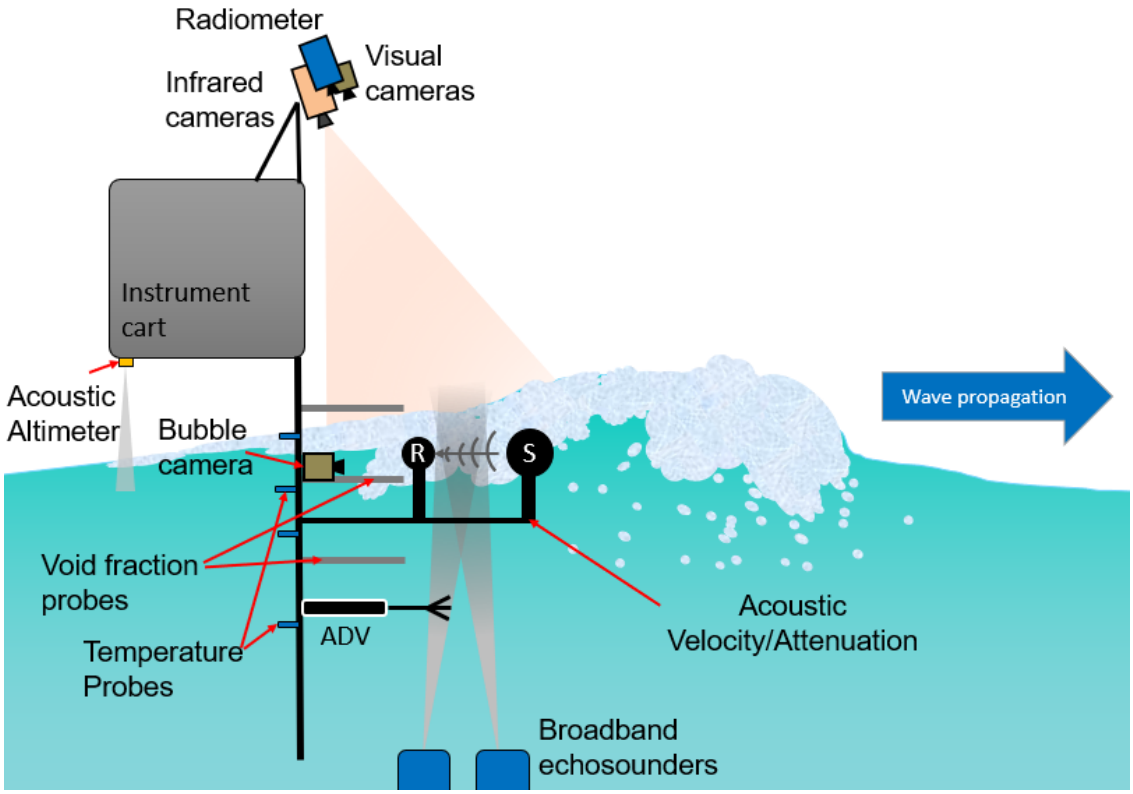

Figure 2.5: Schematic of the instrumentation used at Hinsdale LWF showing infrared and visible cameras, acoustic altimeter, bubble camera, void fraction probes, temperature probes, radiometer, acoustic velocity, and attenuation system, and broadband echosounders. These instruments are all mounted onto a movable instrument cart shown in Figure 2.3. Note that the drawing is not to scale and does not include the wire wave gauges installed in the flume by Hinsdale staff. These wires were mounted to the inside walls of the flume to measure wave height.

acquisition software. When the wavemaker trigger was initiated to create the solitary wave, imagery recording was manually initiated before the wave propagated in front of the measurement location and programmed to stop after three minutes. Camera data and camera metadata, including frame timestamps are saved separately for each camera and run. Each camera's data filename and metadata filename are named as the start timestamp and the camera description.

Acoustic systems were used in this experiment to measure bubble and plume evolution.

A velocity and attenuation system (located 22 cm below the water surface) is used infer bubble size distribution and similar techniques are described in Terrill and Melville (2000). Information about this system is included in Appendix B. Another system is comprised of an upward-facing, bi-static, broadband acoustic scattering system (located 6 ft below the water surface) that measures backscattering from bubble plumes in the water column. The system matches that used in Lavery and Ross (2007) and Bassett et al. (2015) with the transducer pairs operating at 75-130 kHz and 130-200 kHz. These acoustic systems are compared together to develop spatiotemporal measurements of the bubble distributions. The acoustic systems were triggered to run just before a wave-breaking event and for durations of 4-8 minutes. While running, the systems sampled at 4 Hz, but due to a lack of suitable electronics and data acquisition equipment, only one instrument package (e.g., the attenuation system or one echosounder pair) could be operated at a time.

A point radiometer (Heitronics KT-15 longwave radiometer) was used to measure skin temperature, and four temperature probes (Sable Systems TC-2000 Thermocouple Meter-PVC Coated Tip T/C) were used to measure air and in-water temperatures. The temperature probes were taped onto a PVC pipe that was mounted on the back of the instrument cart, and they were positioned to sample just above the water surface and at depths of 5 cm, 20 cm, and 1 m below the surface. The radiometer was mounted with the large DRS with a 14-degree tilt and 4.7 m above the still water surface, sampled at 28 Hz. The temperature probes were acquired under one system, sampled at 5 Hz. The radiometer and temperature probes were programmed to manually start together. If the data acquisition was not manually stopped, a new text file would automatically initiated every hour. Each instrument is outputted into different text files. Each text file was named with the start timestamp and the description of the instrument.

Three void probes (constructed by the Applied Physics Laboratory (APL) at the University of Washington and based on models created by [41]) measured void fraction at different vertical depths: at the water surface, 15 cm below the water surface, and 36 cm below the water surface. Unfortunately, the void probes failed and did not provide usable data. An

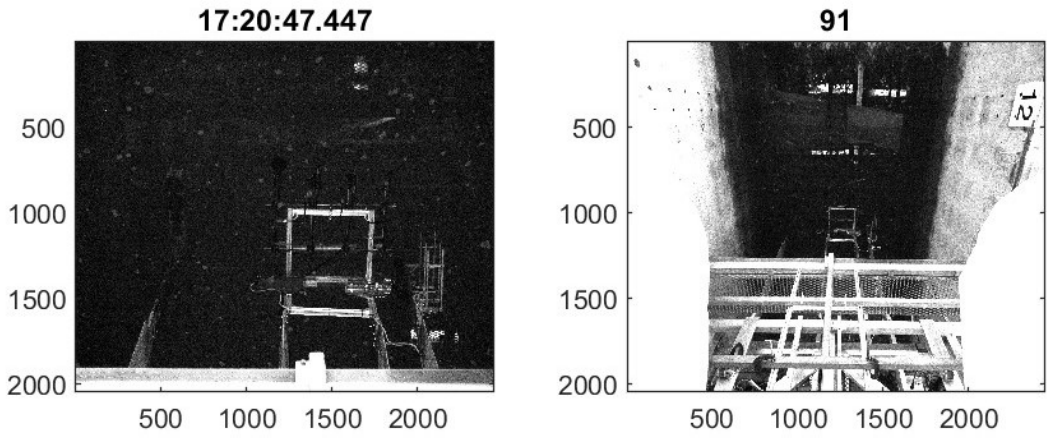

Figure 2.6: These are images of a simultaneous frame of two Blackfly visual cameras: narrow (left) and wide (right) field of view. The timestamp and frame number are shown on top.

ultrasonic altimeter (Banner Engineering S18U) was used to measure the wave profile that was located 1.5 m above the still water and 1.7 m shoreward of the acoustic velocity and attenuation system. The trigger signal to start the wavemaker, which was provided by the Hinsdale Lab, was connected to the void fraction probe data acquisition system, along with the ultrasonic altimeter. This data acquisition system sampled at 1000 Hz. Wire wave gauges were calibrated and provided by the Hinsdale Lab to measure wave height, sampled at 100 Hz and located 28.6, 32.2, 35.9, 39.5, 43.2, 46.9 m away from the wavemaker.

Two Nortek ADVs (a Nortek VectrinoII and a Nortek Vectrino+) were used to measure turbulence; one 20 cm below the water surface and one 142 cm below the water surface, respectively. Both ADVs were programmed using Nortek's software. The Vectrino+ was programmed to acquire data at 100 Hz, while the VectrinoII was programmed to sample at 50 Hz. Each ADV data is outputted in its folders, labeled by model name. The Vectrino+ data file names were labeled under their start timestamp, and VectrinoII data files were labeled ascending. During preliminary testing, the void probes were observed to conflict with noise with the VectrinoII measurements. Thus, only the Vectrino+ was used during the experiment.

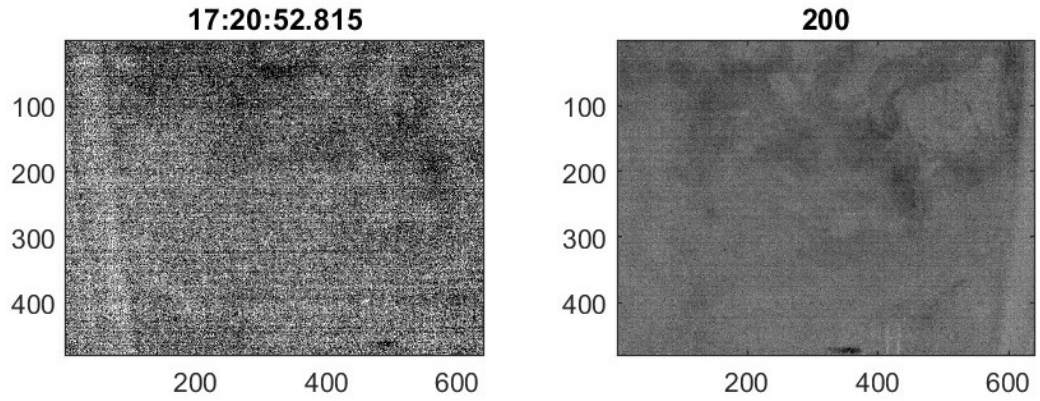

Figure 2.7: These are images of a simultaneous frame from the two DRS infrared cameras: showing the left (left image) and right (right image) side of the flume walls. Lighter shades of gray are warmer and darker shades are colder temperatures. The timestamp and frame number are shown.

After all the sensors were installed on the instrument cart and before test runs started, pictures (e.g. shown in Fig. 2.4) and measurements of the positions of all the instruments were recorded. To be able to take pictures and measurements, the instrument cart was moved close to the beach, where the instruments were at eye-level with the bathymetry. The instruments were 103 inches below the top of the walls of the flume (Figure 2.4). In addition, after the experimentation was completed, prior to removal of the instruments, and the locations of the instruments setup were measured using a Sokkia digital total station.

2.2 Data Collection

2.2.1 Test Procedures

Across the six measurement locations, there were 81 attempts to run waves. To start an experimental run, the wavemaker was initiated with a trigger by a Hinsdale technician in their control room, and a wave was launched in less than 30 s. The wave trigger was recorded by our sampling computer. After the wave passed, we waited for 20-minutes before the next run to allow the bubbles to rise to the surface, the foam to dissipate, the warm skin to be

re-established, and the water surface to settle. A manual log was kept with the datasets to note the times of each experimental run, as well as any significant events, such as the instrumentation configuration change, instrumentation issues, and incomplete runs. Several runs did not result in meaningful data because the wave maker failed to create the wave or the instruments failed to log data properly. Location 1 (front of the cart located 42.2 m from the wavemaker, x= 42.2 m) had five usable runs, Location 2 (x = 44.2 m) had 14 usable runs, Location 3 (x = 46.2 m) had 14 usable runs, Location 4 (x = 48.2 m) had 12 usable runs, Location 5 (x = 50.2 m) had 12 usable runs, and Location 6 (x = 52.2 m) had 13 usable runs. However, due to its position relative to the breaking wave, few bubbles and little foam was observed at Location 1. At Location 6, the data acquisition system for the temperature probes stopped collection after six runs.

To record the observations, two sampling computers were used. The in-situ measurements (void probes, temperature probes, bubble camera, and ADVs) and the remote sensing instruments (radiometer, visual and infrared cameras, and acoustic altimeter) were collected on a desktop. Acoustic measurements (echosounder, attenuation/velocity) were controlled and acquired on a separate computer. Both computers connected to the Internet for clock synchronization using Network Time Protocol and data were recorded in Coordinated Universal Time (UTC). These computers and data acquisition systems were placed on top of the instrument cart, moving with all the instrumentation along the flume.

2.3 Data Processing

Foam coverage, foam decay, the onset of warming foam, bubble plume evolution, wave height, and energy dissipation datasets required further data processing to utilize the necessary metrics for analysis.

2.3.1 Temperature

Radiometer data files are in text files, outputting an epoch time in UTC and raw skin temperature measurement in degrees Celsius. The data was smoothed using a one-minute

moving average. The temperature probe data was smoothed using a five-minute moving average. A -0.3-degree offset was applied to the temperature probe data to match the skin temperatures after a wave breaks and disturbs the skin layer when the skin and the sub-skin measurement (5 cm below the water surface) should be equivalent.

2.3.2 Foam Coverage and Foam Temperature

The visual (hereafter referred to as electro-optical or EO) and thermal infrared (IR) imagery are processed to capture the thermal signal of whitecap foam, capturing plan-view imagery of the large wave flume at six different locations. For the data process, the narrow field of view visual camera was used (shown in the left image in Fig. 2.6) and the right infrared camera (shown in the right image in Fig. 2.7). Raw output files from the cameras come out as data image streams and are reshaped into images. Visual eight-bit data streams are reshaped into 2048x2448 images. To process the visual images, each frame is interpolated to convert the two-dimensional blue-green-green-red Bayer pattern image into a true color image, using the MATLAB Image Processing Toolbox [42] and the function `demosiac`, and converted into grayscale. A threshold based on pixel intensity histogram, similar to that used in Callaghan and White (2008), is applied to detect foam from the background, differentiating foam and non-foamy water and producing a binary image. Lastly, a 20x20 pixel, moving median filter was applied to each frame to remove salt and pepper specks from the image. The metallic instruments and frame structures are misidentified as foam in the EO and IR cameras. A manual outline of the instrumentation was removed from the binary images. The ratio of the detected foam area to the total available of area of the image (excluding the instrumentation area) is recorded as foam coverage fraction for each frame. An example of the EO image processing is shown in Figure 2.8. Infrared images are sampled at a faster rate than visual cameras. To find simultaneous images, the closest timestamp from the infrared camera frames was matched to the corresponding visual camera frames. Infrared 16-bit date image streams are reshaped into 480x640 images. Each infrared frame was demeaned by the mean pixel intensity of that run.

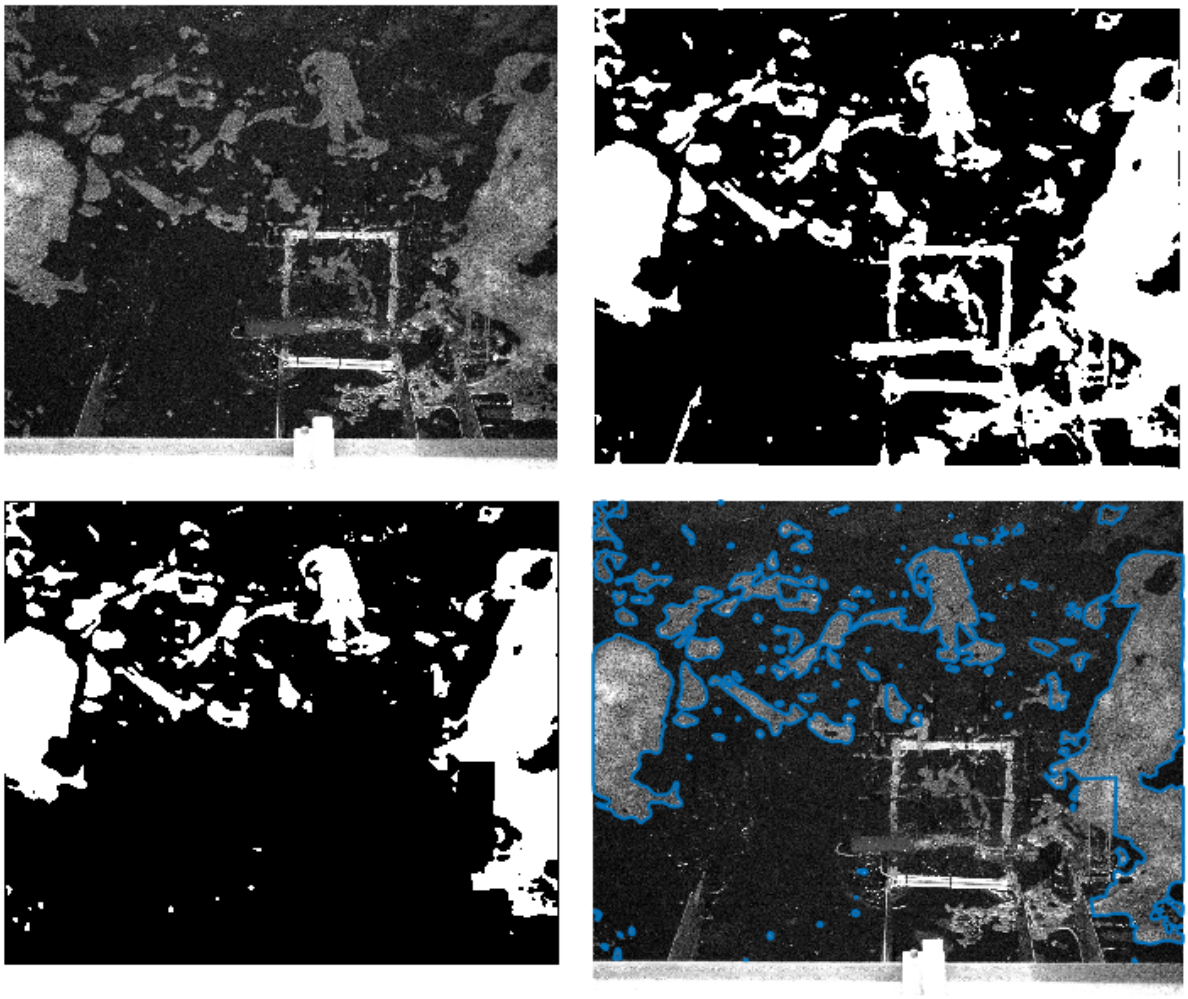

Figure 2.8: The steps of visual (EO) imagery processing. (1: top left) Grayscale image of residual foam. (2: top right) Image is binarized based on a thesholding method[24] to separate foam and non-foam. (3: bottom left) The area containing instrumentation is removed from the binary image. (4: bottom right) The detected foam is outlined in blue.

Since the cameras were positioned at different locations, they have different fields of view (Figure 2.9). To identify the surface foam in the infrared imagery, the visual imagery foam coverage area was mapped based on control points of known objects onto the corresponding infrared image (Figure 2.10). The visual imagery camera had a 2.5 x 3 m view of the tank below. The infrared cameras had a corresponding 2 x 3 m view, after mapping. Based on

the IR and EO images that were overlaid on top of each other, we were able to obtain a relative foam temperature of the detected foam and the non-foam areas, averaging the pixel intensity of the foam coverage area in the infrared image. Based on a previous calibration, the IR images were converted to relative temperature using the response of 100 intensity counts per degree Celsius. Initially, the foam coverage fraction and foam temperature were plotted. Using the time before the foam coverage fraction rapidly increased as a reference, this time was used as the beginning of wave breaking. The time series of foam coverage and foam temperature were shifted to make t = 0 when the wave came into the frame. This was done for each run, at each location and was used to find the ensemble average foam temperature and foam coverage. All the data at a measurement location was averaged and resampled into 0.2 s bins.

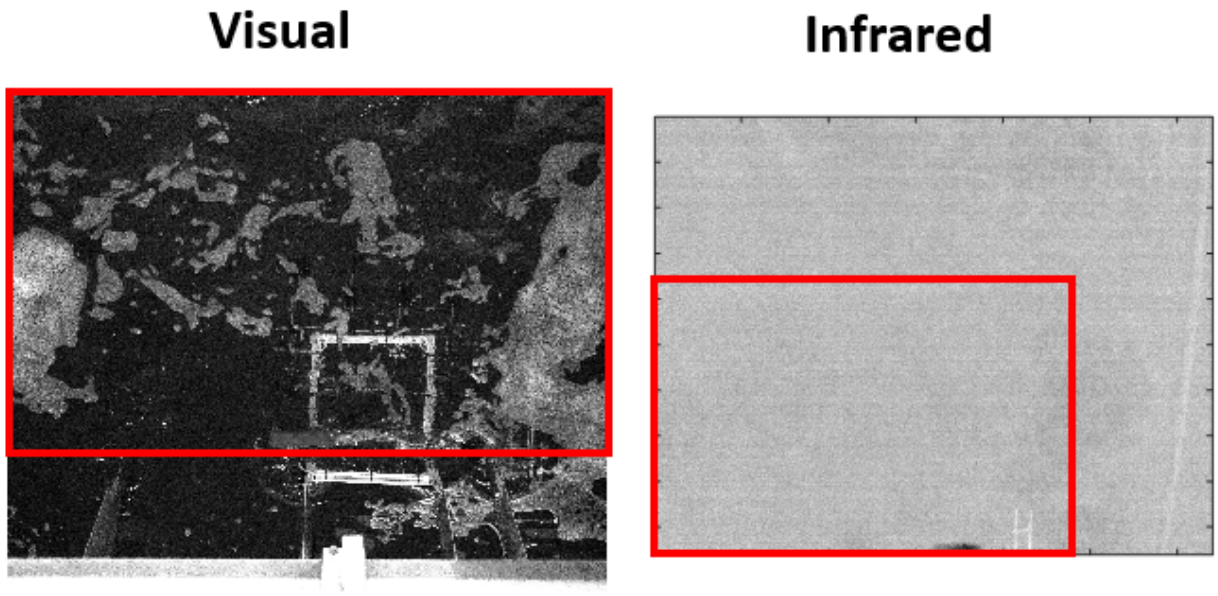

Figure 2.9: (Left) Signal frame taken from the visual camera. (Right) The corresponding infrared frame is taken from the infrared camera. The visual and infrared cameras have different fields of view; in red boxes show the corresponding field of view in each image.

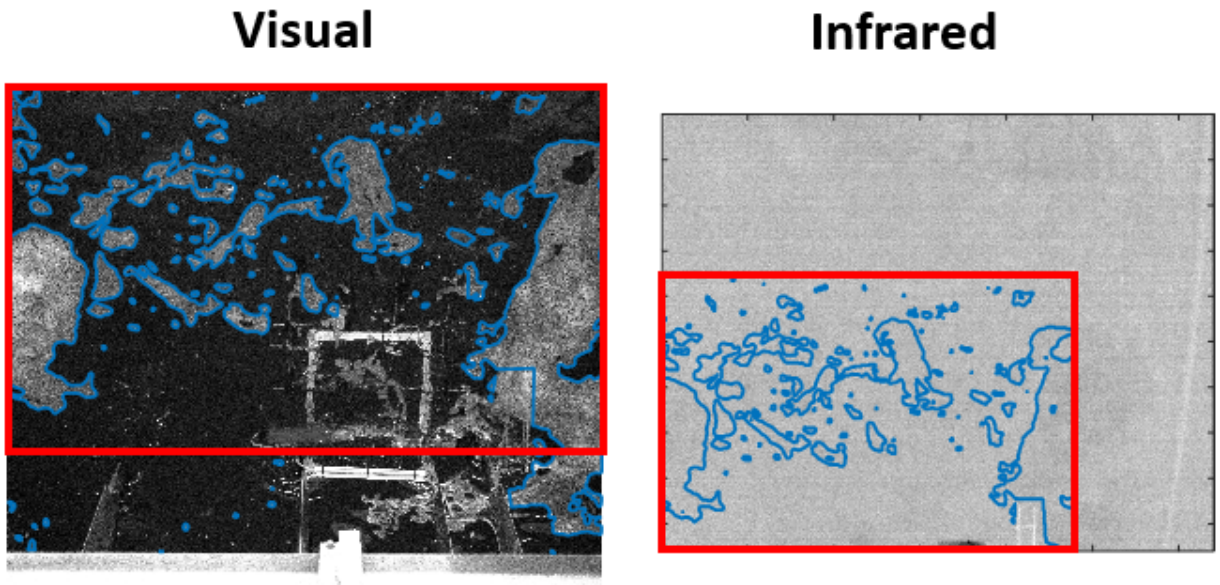

Figure 2.10: The same images from Figure 2.9 with annotations added to highlight the foam. (Left) Using a thresholding method to detect foam, the outline of foam coverage is shown in blue. (Right) The foam coverage area is mapped to fit the same field of view for the infrared image.

2.3.3 Bubble Plume Evolution

Appendix B summarizes the processing of the acoustic attenuation measurements and inferring bubble plume decay time scales (τ_{plume}) and plume depth (d_{plume}). Appendix C describes the bubble camera measurements. The system used a shadowgraphic principle to visualize bubbles in the water and enable bubble size estimation and bubble count.

2.3.4 Wave Height

Calibrated data from the wire gauges mounted to different locations along the tank were collected and quality-controlled by the HWRL. Calibration data was collected while the flume was being filled. Calibration data, raw data, and calibrated data in .txt, .dat, and .mat formats were available for processing. These datasets were labeled by the date, type of wave, and x-location. Each .mat file contained data for each experimental run. Calibrated

data was given in volts and directly corresponded to a height in m/volt. I compiled all the trials into single arrays for the six wave gauges and time. With start and end timestamps, the arrays were separated by location. After removing data from incomplete breaking waves, maximum wave height was recorded for each run. To find the ensemble maximum wave height, the maximum wave height from a location was averaged together.

The ultrasonic altimeter data was collected under the same acquisition system as the void probes, outputting the data into text data. These measurements directly measure the distance of the closest object. Raw data was organized into the different experimental run indexes. By the run index, the data was organized by location, and the ensemble maximum wave height for each location was calculated, identical to the wire wave gauge processing.

Chapter 3

RESULTS

The results are presented in five sections: temperature measurements, foam fraction coverage and decay, foam temperature evolution, bubble plume evolution, and energy dissipation. These parameters evaluate the system's relevant characters and present the dynamics of the breaking wave and its subsequent foam and bubble plume.

3.1 Temperature

Temperature probes and radiometer measurements show temperature at different vertical locations. There were four temperature probes, measuring air and 5 cm, 20 cm, and 1 m below the water surface. Using the radiometer, the skin temperature was recorded. An example of temperature measurements from one day is shown in Figure 3.1.

The air temperature measured above the water surface, increased from approximately 21 $^{\circ}C$ in the morning to approximately 23 $^{\circ}C$ in the late afternoon. Over the entire week of measurements, air temperature did not exceed the range between 18 and 25 $^{\circ}C$. This range wass between the outside low- and high-temperature range, shown in Table 3.1 taken

Date	High Temperature ($^{\circ}C$)	Low Temperature ($^{\circ}C$)
8/8	36	11
8/9	28	12
8/10	31	19
8/11	27	9
8/12	31	9

Table 3.1: Table of high and low temperature for the dates of measurements in Corvallis, Oregon. These measurements are taken from Hyslop Weather Station by the College of Agricultural Science at Oregon State University[43]

from a local weather station. Over this same period, the measurements in the water column remained stable at about 19.5 $°C$. Skin temperature varied with time, driven by the wave breaking. As a wave disrupts the skin layer, the skin temperature, typically starting at 19.8 $°C$, rapidly decreases to about 19.5 $°C$. Turbulence and mixing cause foam and non-foamy water to be at the same temperature as the water below the skin. As foam dissipated and the skin layer reformed, the skin temperature then slowly increased until reaching a temperature similar to before breaking after a period of ten minutes or more.

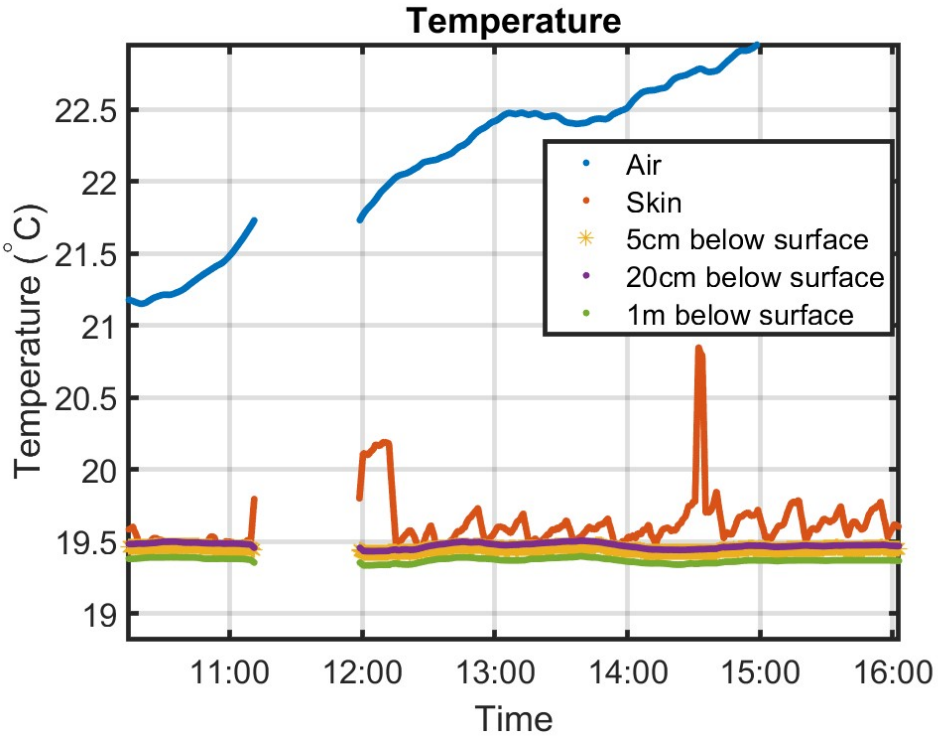

Figure 3.1: One day (Wednesday, August 10, 2022) of temperature measurements from the temperature probes and radiometer. The time is in Pacific Standard Time. The temperature was measured at above the water surface (air), skin temperature (using the radiometer), and 5 cm, 20 cm, and 1 m below the water surface.

3.2 Foam Coverage Fraction and Foam Decay

Foam coverage fraction A, is the fractional area of surface foam that covers the available field of view, as described previously. Figure A.1 shows the foam coverage fraction time series for Locations 1-6. Foam decay lifetime τ_{foam} is calculated from foam coverage fraction time series. Equation 3.1[19] relates foam decay time scales, τ_{decay}, to foam coverage area fraction A_{foam}, maximum foam coverage area fraction A_{max}, and time t, according to Equation 3.1:

$$A_{foam} = A_{max} exp\left(\frac{-t}{\tau_{decay}}\right). \tag{3.1}$$

For each run, the foam decay time scale is calculated from the foam coverage fraction in natural logarithmic space, according to Equation 3.2:

$$ln(A_{foam}) = ln(A_{max}) - \frac{t}{\tau_{decay}}. \tag{3.2}$$

In Equation 3.2, the negative inverse of the slope is the e-folding foam decay time scale from maximum foam coverage τ_{decay}. Total foam decay lifetime τ_{foam} is defined to include the time from wave breaking to maximum foam coverage area and the time from maximum foam coverage to foam exponential decay, as in [25]. An example run with the fit to Eqn. 3.2 is shown in Figure 3.2. On the right plot of Fig. 3.2, at wave breaking t=0, foam coverage starts at zero. The foam coverage rapidly increases to 0.8 foam coverage fraction within 0.4 s. During this time, foam propagating with the breaking wave saturates the field of view, appearing 80 percent white. Foam coverage immediately starts to decay, taking 15 s to completely dissipate. High levels (> 0.6 foam coverage fraction) of foam coverage persist for approximately 2 s. On the left plot of Fig. 3.2, the linear fit slope is approximately -0.25. Therefore, according to Eqn. 3.2, the τ_{decay} is 4.0 s, and τ_{foam} is 4.4 s.

For each measurement location, foam coverage starts at approximately zero. Foam coverage does not always start or end at zero foam coverage because excess noise from residual foam that did not dissipate completely or overhead reflection that appeared white in imagery. For all locations, foam coverage fraction rapidly (within 0.3 to 0.4 s) jumps to maximum levels where the foam coverage fraction is close to one, persists at a high level of foam coverage

(> 0.6 foam coverage fraction) for a few seconds, then slowly decays to pre-breaking levels of foam coverage.

Foam decay varied across locations (see Figure A.1) with the following characteristics:

- Location 1: Foam decays quickly, within 3 s, and returns to pre-breaking values at t = 5 s. However, this short lifetime is caused by foam advecting out of the field of view.
- Location 2: Foam decay takes longer than most locations (except Location 6). High levels of foam coverage persist for approximately 3.5 s and return to pre-breaking values at t = 11 s; the foam decay lifetimes occur around 7.6 s on average.
- Location 3: high levels of foam coverage persist for approximately 3.5 s and return to pre-breaking values at t = 8 s. Foam coverage appears bimodal, having two local peaks at t = 0.7 s and t = 2.7 s; the foam decay lifetimes occur around 4.3 s.
- Location 4: High levels of foam coverage persist for approximately 2.3 s and return to pre-breaking values at t = 8 s; the foam decay lifetimes occur around 4.6 s on average.
- Location 5, high levels of foam coverage persist for approximately 7 s and return to pre-breaking values at t = 11 s. Foam coverage appears bimodal, having two local peaks at t = 0.7 s and t = 3.9 s. Foam decay lifetimes occur around 4.3 s; the foam decay lifetimes occur around 6.2 s on average.
- Location 6, high levels of foam coverage persist for approximately 4 s and return to pre-breaking values at t = 15 s. The foam coverage curve is not as smooth as the other locations, consisting of many smaller local peaks relative to the maximum foam coverage. Also, the foam decay lifetimes occur around 8.3 s on average.

At Locations 3 and 5, the bimodal behavior suggests large areas of foam advecting in and out, but dissipating, in the field of view. At Location 6, the local peaks also suggest advection; however, observations during the experiments suggest additional motion (e.g., seiching) is contributing to this result. Although the rapid increase in foam coverage, foam persistence, then eventually, decay patterns were generally consistent between runs at specific locations within the tank, there were differences in foam coverage observed spatially along the tank, which are discussed in greater detail in Chapter 4.

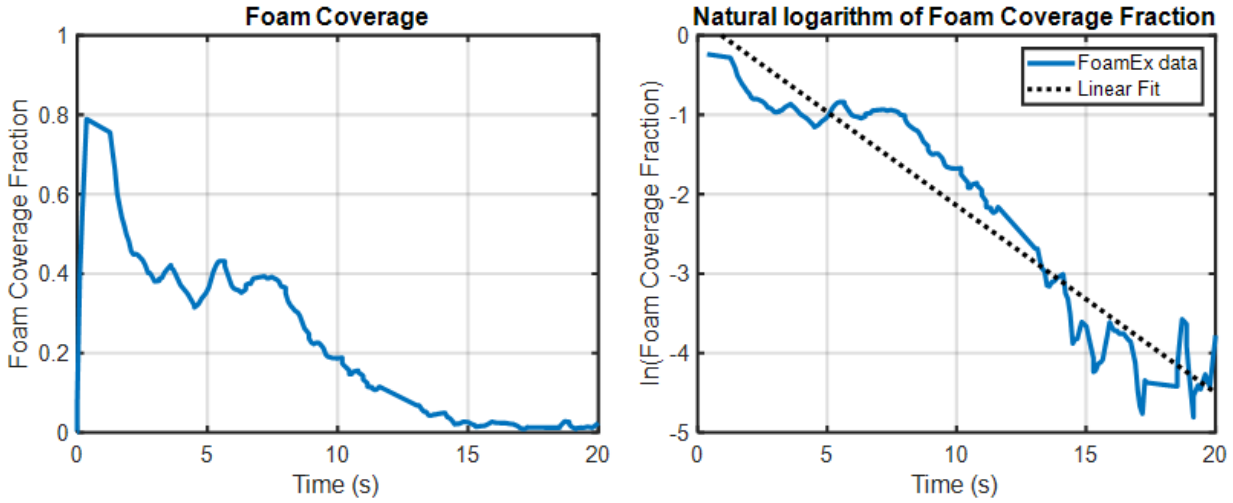

Figure 3.2: (Left) An example run from Location 6 of foam coverage time series. (Right) The natural logarithm of foam coverage. The dashed line shows a linear fit, which is related to the total foam decay time scale by Equation 3.2.

Figure 3.3 shows the time scales for foam decay measured at various positions along the tank. This plot does not show Location 1 (2.7 m distance from breaking point (DFBP)), because there is a lack of viable runs to do any statistical analysis or inference. This lack of data is attributed to measurements, which were taken right when the wave began to break so little foam was generated within the field of view of the cameras. For each measurement location, there is a large spread of values for foam decay τ_{foam} that is on the order of $\pm 50\%$ of the mean value. At Location 2 (5.8 m DFBP), the mean τ_{foam} was approximately 7.7 s and was the second highest value observed along the tank. Locations 3 to 6 (7.8, 9.8, 11.8, and 13.8 m from DFBP), in contrast, show increasing τ_{foam} values, increasing from approximately 4 s to greater than 8 s as the wave propagates onshore.

3.3 Foam Temperature and the Onset of Warming

Foam temperature was measured through visual and infrared imagery. After the foam coverage area was detected by the visual cameras, the foam coverage area was mapped on the

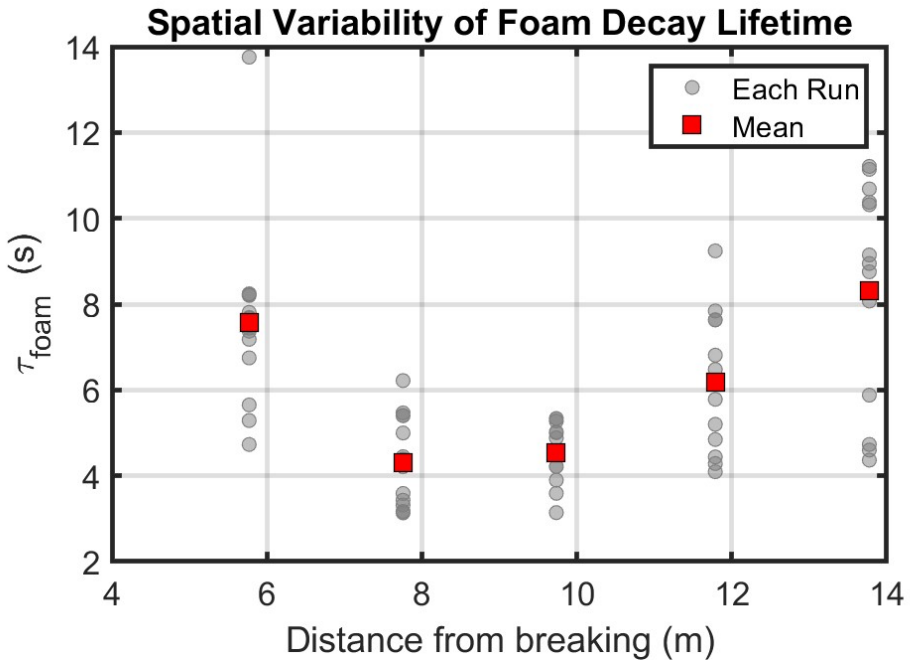

Figure 3.3: Spatial Variability of foam decay lifetime τ_{foam}.

infrared images to determine the relative temperature of foam water to non-foamy water. The time series of the relative temperature of foam for all the measurement locations is shown in Figure A.2. There is considerable scatter between each run in the relative foam temperature for each run. However, the relative foam temperature trends typically follow a similar pattern: first, at wave breaking, t = 0, relative foam temperature is approximately 0°, next, a rapid decay occurs almost instantaneously (less than a second) after breaking, followed by a plateau period, and a subsequent gradual increase in relative temperature. The foam temperature does not return to pre-breaking temperatures, because the foam dissipates within 15 s. In the example time series of relative foam temperature (Fig. 3.4), it takes 0.4 s from wave breaking to the start of the plateau period. The plateau period lasts for 1.1 s; therefore, the onset of warming time scale τ_{warm} is 1.5 s. From wave breaking to the rapid decay period is on the order of 0.4 s, similar to the period from wave breaking to foam coverage saturation. The length of the plateau period is dependent on the measurement location.

The minimum temperature that relative foam temperature reaches the bulk temperature of the water.

To find the onset of the warming time scale, t_{warm}, a piecewise fit to relative foam temperature time series is used. The piecewise function has three linear parts: a linear decay, a constant temperature, and a linear increase. The decay line represents the period associated with the disruption of the warm skin by the breaking wave. The constant temperature period represents the period when rising bubbles are resupplying the surface foam. As the rate of renewal of the foam by rising bubbles decreases, warming of the skin is no longer inhibited and foam temperature increases to the original temperature of the warm skin. This process is similar, but reversed to that typically observed previously in nature [36], due to inward direction the direction of heat flux [28]. In more natural environments, cool skin and cooling foam are more common as depicted in Figure 1.3. Looking at the spatial variability of the warming time scale, there is a large spread for each location of measure, however, the onset of warming, t_{warm} increases from 2.0 to 5.5 s from 5.7 m to 13.7 m DFBP, depicted in Figure 3.5.

3.4 Bubble Plume Evolution

Two acoustic transducers were in the water column to measure excess attenuation (α) to infer bubble plume decay time scale τ_{plume}. Additional details about the methodology, processing, and inversions are described in Appendix B. The spatial variability of bubble plume decay time scale τ_{plume}, shown in Figure 3.6, does not have a noticeable trend. Not enough bubbles were present at Location 1 to significantly affect excess attenuation α. Plume decay time scale τ_{plume} starts second farthest offshore at 5.8 m DFBP (Location 2). As the τ_{plume} increases in DFBP, the value oscillates low and high from 3.8 s (at 5.8 m DFBP), 6.7 s (at 7.8 m DFBP), 2.9 s (at 9.7 m DFBP), 8.5 s (at 11.8 m DFBP), and 3.2 s (at 13.8 m DFBP).

Using the bubble camera system, the bubble size distribution is measured, shown in Figure C.2. The time series of bubble size distribution is shown as histograms for each

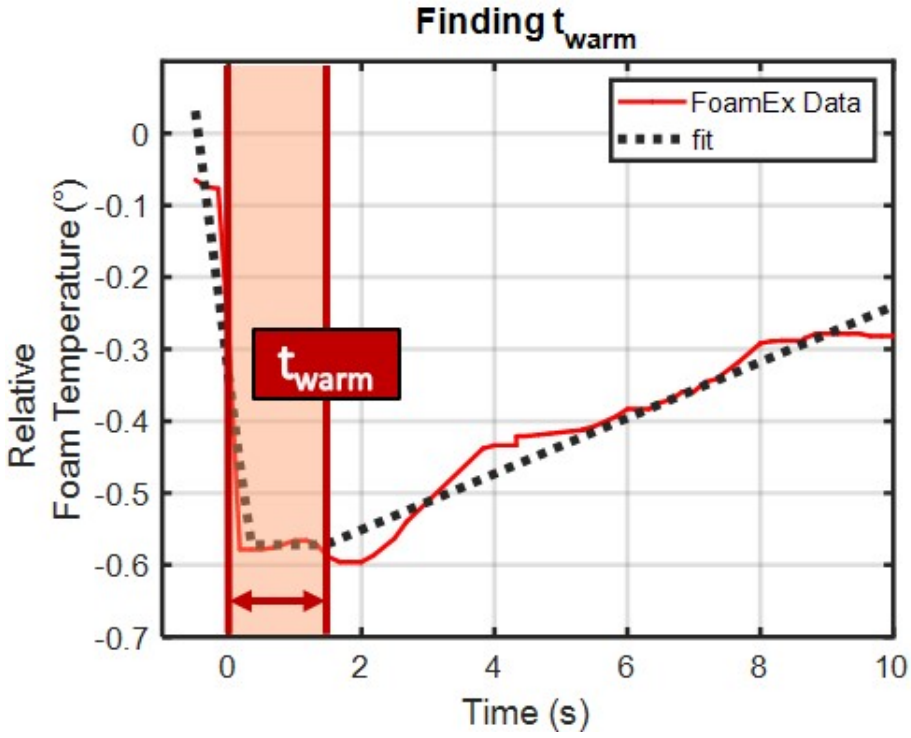

Figure 3.4: An example of time series of relative foam temperature of a run. In red, the relative foam temperature is plotted. A piecewise linear fit was applied to the time series to find the onset of warming t_{warm}, starting from t = 0 until the time when relative temperature starts to increase.

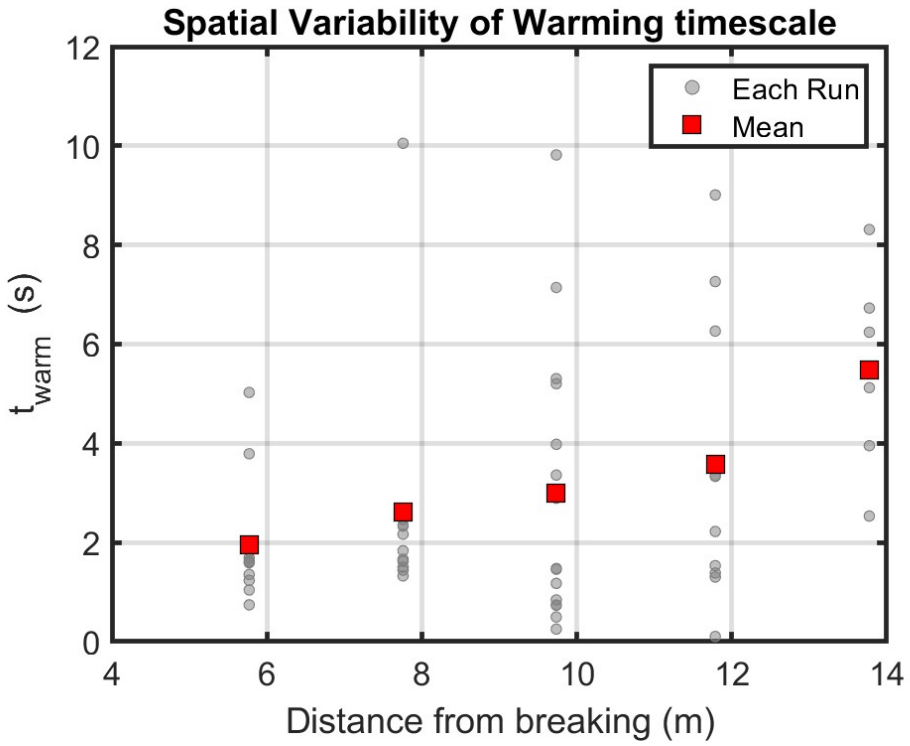

Figure 3.5: Spatial Variability of foam decay time scale t_{warm}.

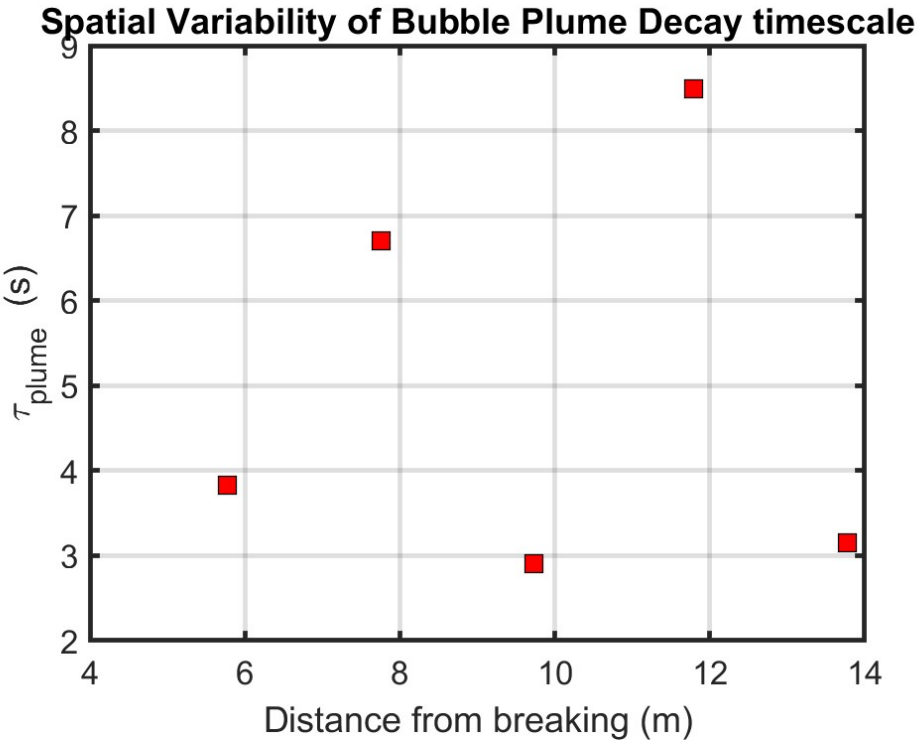

Figure 3.6: Spatial Variability of bubble plume decay time scale τ_{plume}.

measurement location, shown in Figure 3.7. From offshore to onshore, the histograms show that more larger bubbles stay in the water column. At all locations, small (radius $a < 1$ mm) and large ($a >$1 mm) bubbles are present. However, at Location 1 and 2, a small number of bubbles are present ($<$ 100 bubbles), and stay in the water column for 6 s and 8 s, respectively. The number of bubbles increases with DFBP, and small bubbles stay in the water column for longer periods. At Location 6, small and large bubbles are present 30 s after breaking, in large quantities ($>$ 100 bubbles). These histograms were also used to calculate the total void volume by radius, or the volume of air in the field of view, using Equation 3.3,

$$V = \frac{4}{3}\pi r^3. \tag{3.3}$$

A time series of void volume is shown in Figure 3.8. Note that at the beginning of each time

series, there are very few bubbles in the histograms; however, it is not representative of the true bubble distribution. In the initial breaking, there are enough bubbles to nearly fully obscure the image view and the bubble detection algorithm cannot detect single bubbles. Fig. 3.8 shows that bubbles stay in the water column with DFBP. However, Location 6 has the highest value of void volume but the void volume time scale is shorter than Location 5, suggesting that there is a large number of bubbles rising to the surface quickly due to their high buoyancy. From Locations 1 to 3, the void volume is relatively similar but stays in the water column longer with increasing DFBP, suggesting that more bubbles are injected deeper into the water column. Looking at the bubble results from the acoustics and bubble camera, there is not an obvious trend in spatial variability, which is discussed in greater detail in Chapter 4.

3.5 Wave Height and Energy

Maximum wave height (MWH) was measured with the wire wave gauges and ultrasound altimeter along the tanks (Figure 3.9). The wire wave gauges are positioned relative to the breaking point. They show the wave height increasing due to shoaling over the bar (when DFBP is from -11 to -3.7 m, MWH increases from 0.9 to 1.2 m), and the wave breaks between -3.7 and 0 m DFBP. MWH decreased from 1.2 to 0.8 m, at -3.7 to 7.3 m DFBP. The ultrasonic altimeter, which only measured at positions onshore relative to the breaking point, shows wave is decreasing in MWH (MWH decreases from 1.4 to 0.4 m at 3.7 to 13.8 m DFBP). The wire wave gauges and ultrasonic altimeter have different wave height values for similar locations due to their sensitivity to void fraction. Wire wave gauges measure capacitance and cannot detect water heights with high void fractions such as splash-up and bubbly water. The ultrasonic altimeter is sensitive to high void fraction water and will record higher values of wave height. Using the total energy equation for a solitary wave [44]:

$$E = \frac{8}{3}\rho g d^3 \gamma \sqrt{\frac{\gamma}{3}}, \tag{3.4}$$

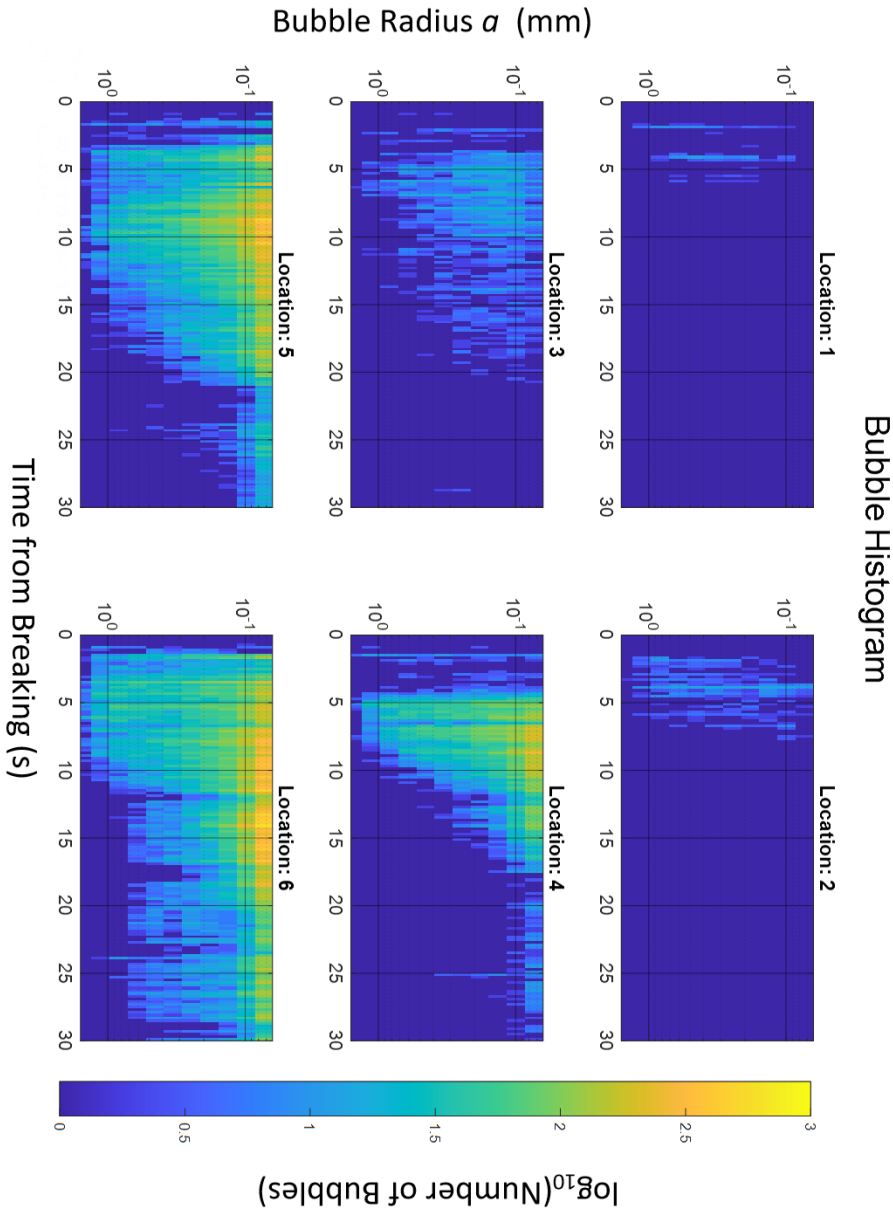

Figure 3.7: Bubble Size Histogram for Locations 1, 2, 3, 4, 5, and 6.

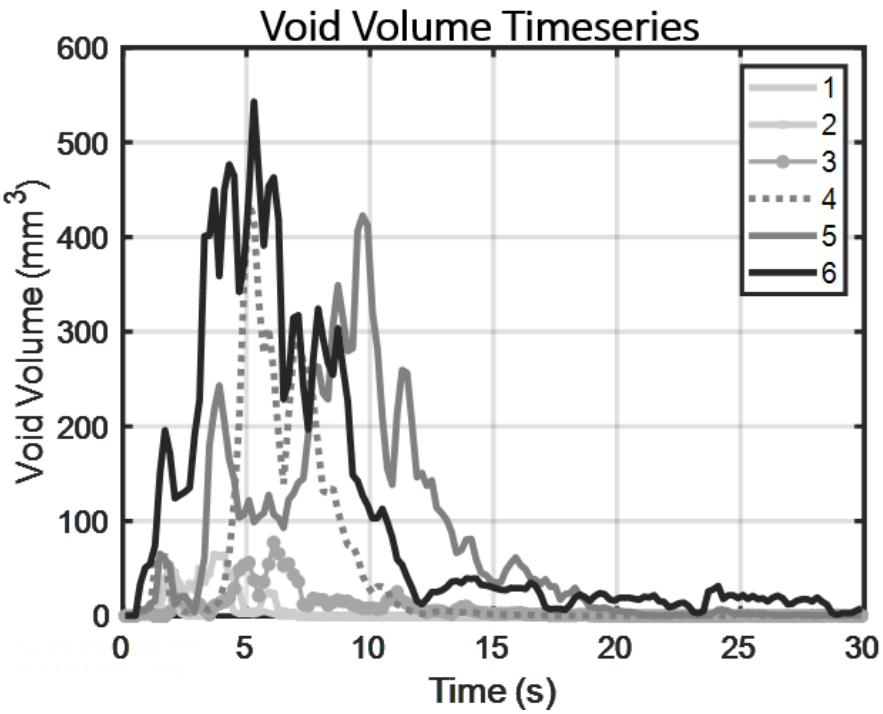

Figure 3.8: Bubble Void Volume time series for Locations 1, 2, 3, 4, 5, and 6.

where ρ is density, g is gravity, d is water depth, γ is defined by Eqn. 1.11, and phase speed for a solitary wave:

$$C = \sqrt{g(d+H)}, \tag{3.5}$$

where H is wave height. Energy dissipation rate per unit crest length ϵ [W/m] can be calculated, using:

$$\epsilon = \Delta E \frac{C}{\Delta x}, \tag{3.6}$$

where ΔE is the difference of total energy between two points and Δx is the distance between two points. We calculated the dissipation from adjacent pairs of wave height measurements separately from each instrument. From the spatial variability of energy dissipation rate results in Figure 3.10, it is difficult to conclude any trends with ϵ if using all the points. The first two data points from the ultrasonic altimeter are judged to be too high or too low to be realistic. Therefore, these points are ignored, revealing a grouping trend. Close to the

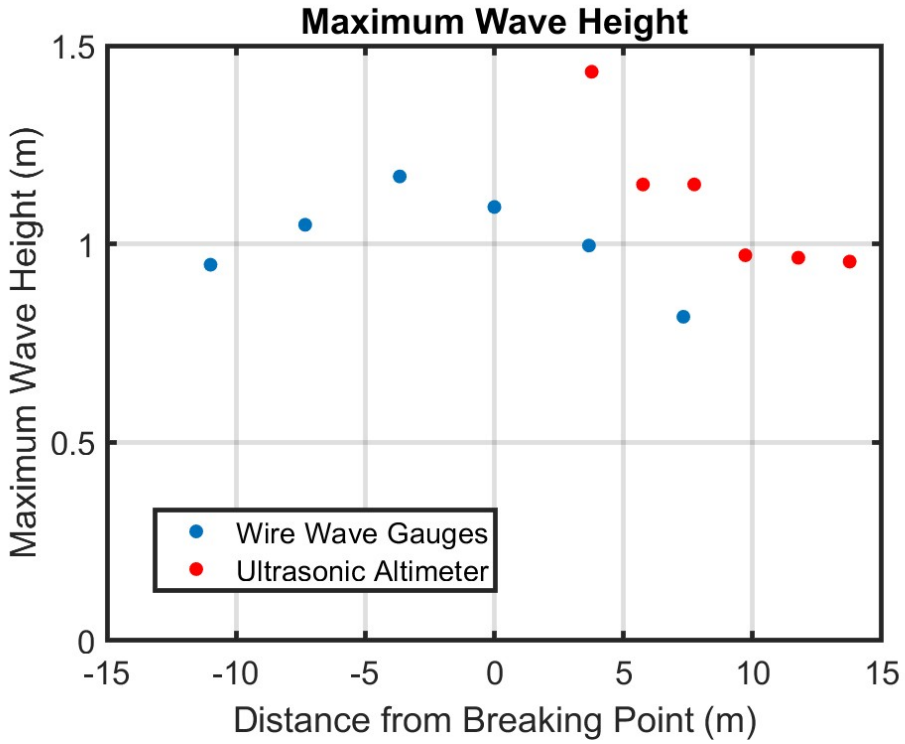

Figure 3.9: Maximum wave height at different locations along the flume, measured with wire wave gauges and ultrasound altimeter.

breaking point, energy dissipation rate is high (on the order of 10^1 or 10^2 W/m), and close to onshore, the energy dissipation rate is low (on the order of 10^{-1} W/m).

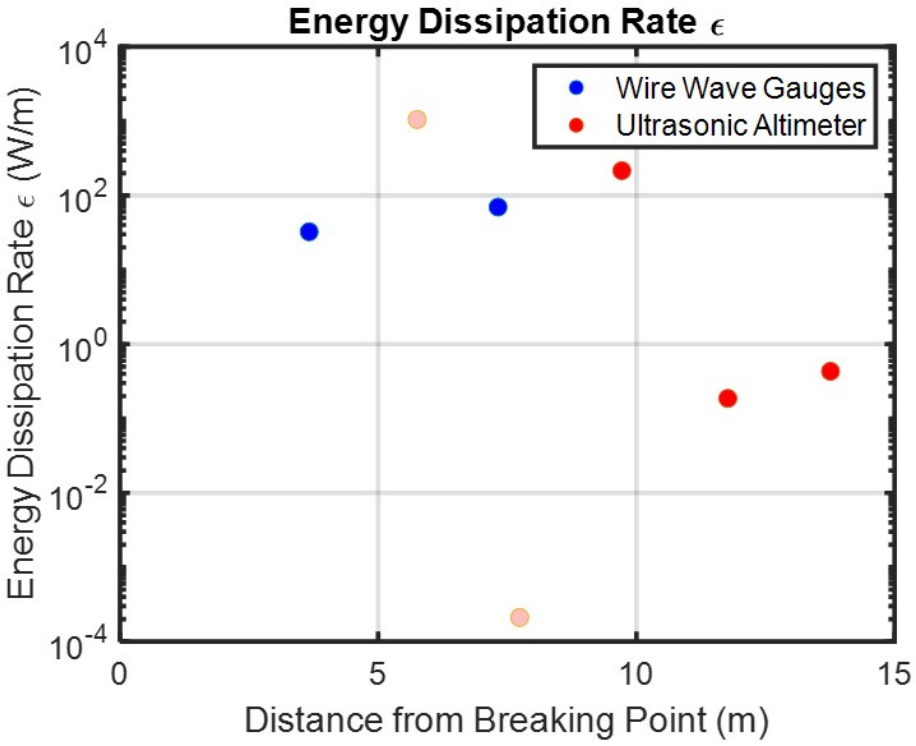

Figure 3.10: Energy dissipation rate at different locations along the flume, measured with wire wave gauges and ultrasound altimeter.

Chapter 4

DISCUSSION

The FoamEx project is an extension of MCJ2021, scaling up the observations of wave breaking and subsequent processes, such as bubble plume and foam generation and energy dissipation, to a field-scale experiment with higher dynamic range. We attempt to verify or disprove the hypothesis that spatial variability of foam temperature evolution can be used as a proxy for bubble plume evolution and spatial variability. To do so, we look at the spatial variability of energy dissipation rate and the time scales of foam temperature, foam lifetime, and bubble plume lifetime.

4.1 Spatial Variability

The spatial variability of the onset of warming time scale t_{warm}, the foam decay time scale τ_{foam}, bubble plume decay time scale τ_{plume}, and energy dissipation rate ϵ was described in the Results section. Figure 4.1 compares all these variables. A positive correlation between t_{warm} and distance from the break point was observed. τ_{foam} generally had a positive correlation with distance from the break point, except for Location 2 (approximately 6 m DFBP). In contrast, τ_{plume} had no clear spatial pattern. Higher dissipation rates were observed close to the break point, and far from the break point (close to shore), ϵ was lower. There was a large amount of energy dissipation that took place between Location 4 and 5 (approximately 10 to 12 m DFBP). Energy dissipation rate may affect the temperature, foam, and bubble plume time scales. To further investigate, comparisons between the four variables were conducted.

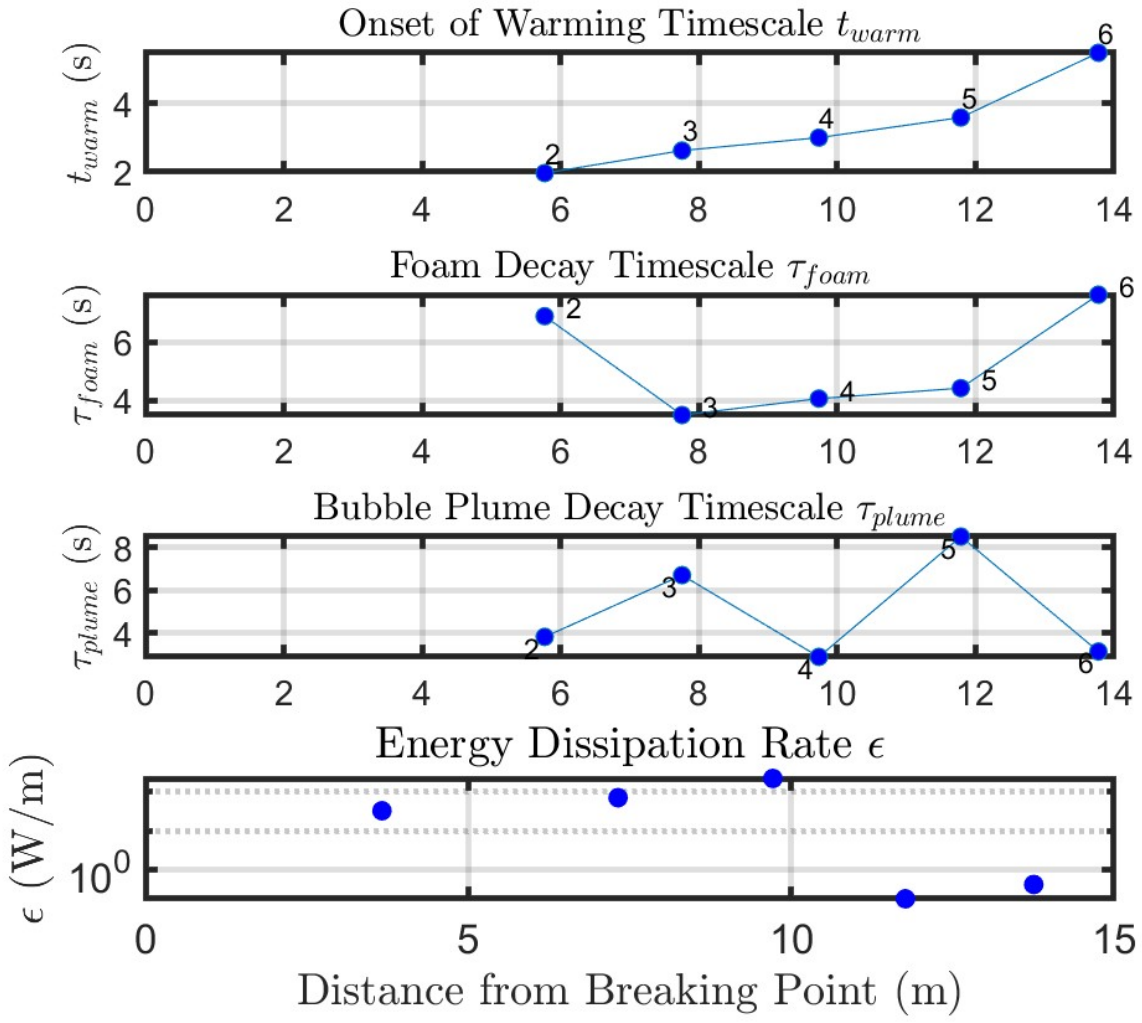

Figure 4.1: Plots of the spatial variability of the Onset of Warming t_{warm}, Foam Decay τ_{foam}, Bubble Plume Decay τ_{plume}, and Energy Dissipation Rate ϵ time scales. Each symbol shows the ensemble mean from each location, not showing spread in the experimental runs.

4.2 Time scales

4.2.1 Warm and Cool Foam

Often in nature, an outward heat flux driven by evaporative cooling results in a cool skin at the air-sea interface. In this experiment, observations suggest warm skin formation due

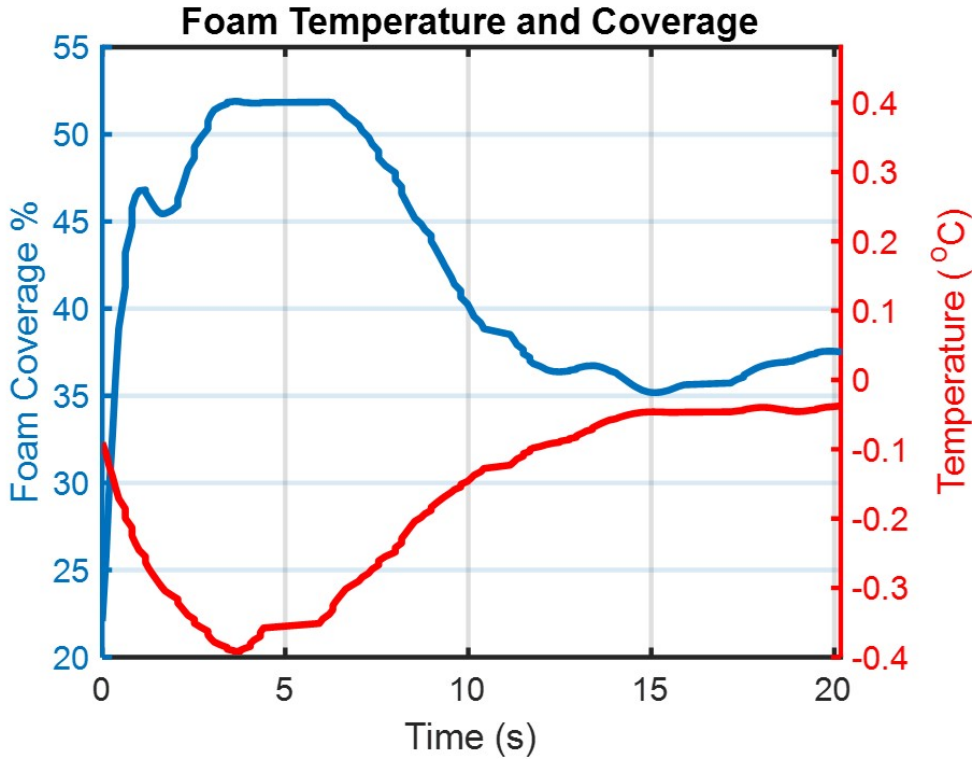

Figure 4.2: An example run of foam temperature and foam coverage for comparison to the conceptual model in MCJ2021. Foam coverage percentage is on the left y-axis and plotted in blue. Foam temperature is plotted on the right y-axis in red.

to warmer air over cooler water, shown in Fig. 3.1. In comparing the conceptual model in Fig. 1.4 to an example run, there is an opposite signal in foam temperature, shown in Figure 4.2. Similar to the results in MCJ2021, as a wave breaks foam coverage rapidly increases and exponentially decays. However, here, foam temperature decreases and reaches a fixed minimum (the temperature of the bulk temperature beneath the water surface) for some time as bubbles supply to surface foam. Once the rate of bubble supplying foam is less than the rate of warming, the foam will warm until all the foam is dissipated. Eventually, the warm skin will reform. The opposite temperature variability, with cooling foam, was observed by MCJ2021.

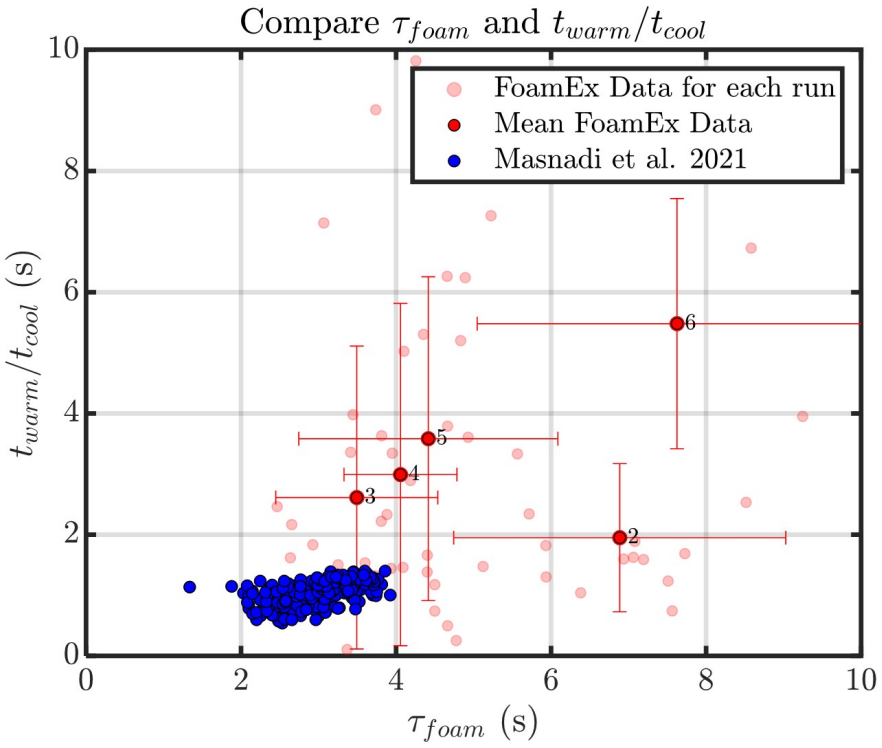

Figure 4.3: Temperature time scale t_{warm} or t_{cool} versus visible foam lifetime τ_{foam}. Each symbol represents one experimental run. Blue symbols are from MCJ2021. Light red symbols are from this FoamEx project. The ensemble mean from each measurement location is symbolized by opaque red dots with the corresponding location label.

4.2.2 Time Scales

In Figure 4.3, it compares t_{warm} or t_{cool} versus τ_{foam} from MCJ2021 and this FoamEx project. There is not a consistent correlation between the two datasets, however, both saw a positive correlation between the temperature time scales and foam decay time scales, which is consistent with other previous work [19]. Both have a trend of foam decay time scales that are relatively long compared to the temperature time scales. The scatter in the FoamEx dataset could be due to the increase in dynamic range and spatial variability. This experiment also used freshwater with added surfactant to mimic saltwater foam properties, and the use of surfactant can affect of longevity of the foam lifetime, stabilizing the surface foam

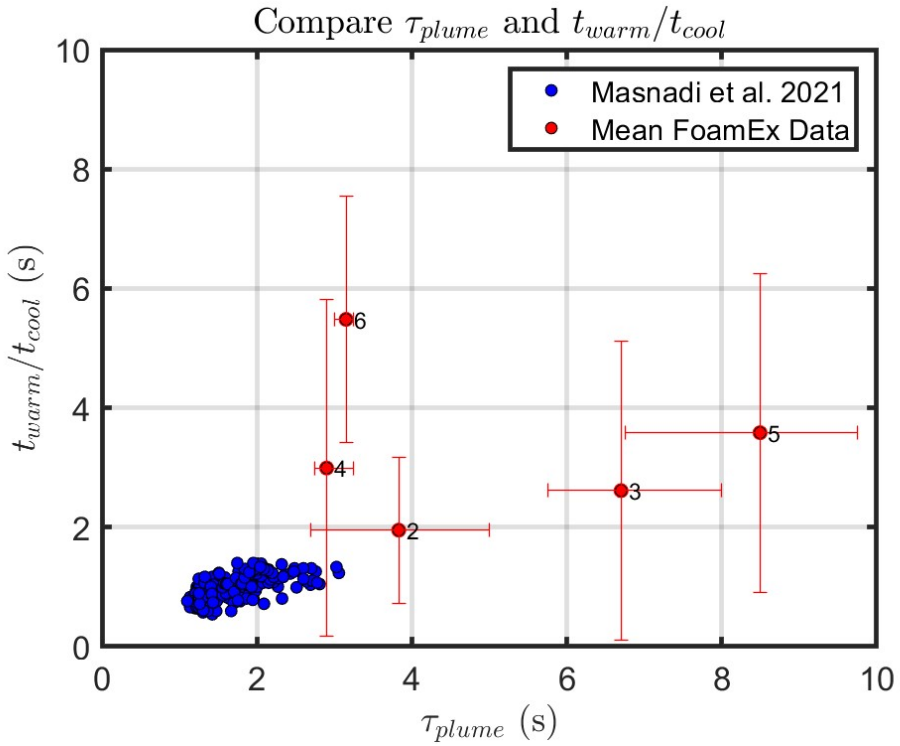

Figure 4.4: Temperature time scale t_{warm} or t_{cool} versus bubble plume time scale τ_{plume}. Each blue symbol represents one experimental run from MCJ2021. From the FoamEx Project, the ensemble mean from each measurement location is symbolized by opaque red dots with the corresponding location label.

and delaying foam dissipation.

MCJ2021 found a strong and roughly linear correlation between the temperature time scale t_{cool} and the bubble plume time scale τ_{plume}, suggesting the onset of cooling can be used as a proxy for bubble plume evolution [28]. However, in FoamEx, there is not a clear linear correction between t_{warm} and τ_{plume}, shown in Figure 4.4. From the MCJ2021 data, there is a positive linear correlation between foam lifetime and bubble plume lifetime, but FoamEx foam lifetime τ_{foam} is not simply correlated with bubble plume lifetime τ_{plume}. In Fig. 4.4 and 4.5, the data is grouped by τ_{plume}. Locations 2, 4, and 6 have shorter plume time scales, and Locations 3 and 5 have longer plume time scales. This suggests different stages of wave breaking and its resulting bubble plume dynamics and evolution have a strong effect

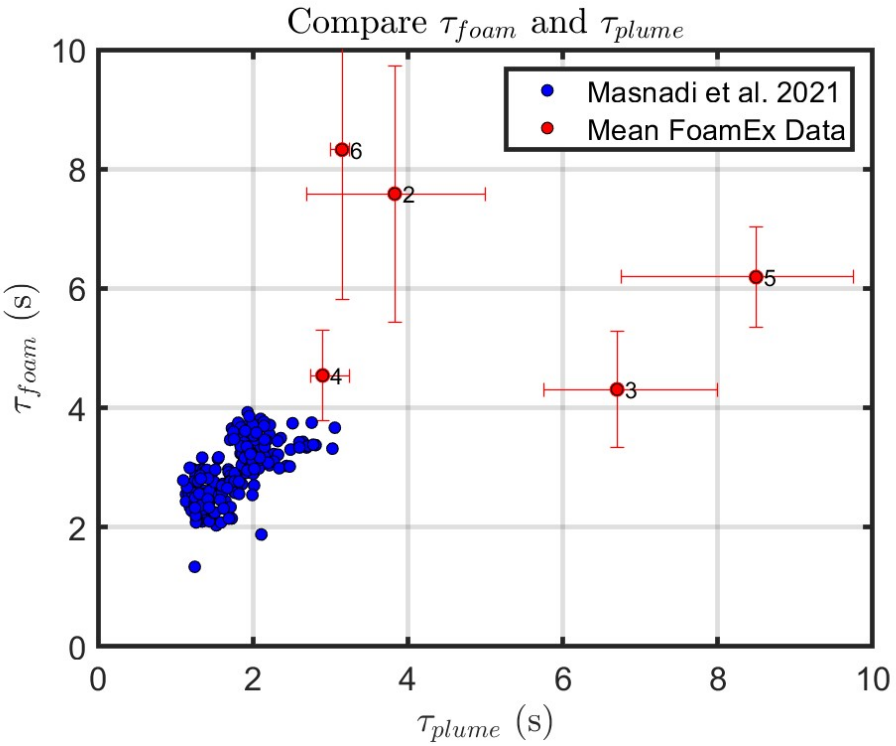

Figure 4.5: Visible foam lifetime τ_{foam} versus bubble plume time scale τ_{plume}. Each blue symbol represents one experimental run from MCJ2021. From the FoamEx Project, the ensemble mean from each measurement location is symbolized by red dots with the corresponding location labeled.

on foam time scales and temperature time scales. The 1.5 s offset that was added to τ_{plume} values to consider the distance from the transducers to the water surface (22 cm) could affect data correlation with MCJ2021, but it does not affect the grouping of the measurements. In addition, MCJ2021 observed that as energy dissipation increases, τ_{plume} and t_{warm} also increase, inferring τ_{plume} and t_{warm} as proxies for energy dissipation. However in Fig. 4.4, as t_{warm} increases with DFBP, energy dissipation rate decreases. In the FoamEx experiment, we cannot confirm the use of τ_{plume} and t_{warm} as proxies for determining the spatial variability in energy dissipation, yet.

Figure 4.6: Images of after wave breaking of instrumentation at Location 4. The left image is a back view of the instrumentation. The right image is a front view of the instrumentation. These images were taken of different runs. However, the locations of the bubble plume injection are similar for each run. Corresponding arrow colors are similar locations of bubble injection.

4.3 Bubble Injection

To look at the effects of spatial variability of bubble plume evolution on the foam and temperature time scales, we examine the locations of bubble injection from the solitary wave. MCJ2021 observed two distinct bubble plumes and foam patches at the surface. The two different plumes have different intensities and injection depths, resulting in different spatiotemporal evolution. In FoamEx, the one-meter solitary wave was a plunging wave that created a similar effect creating multiple plumes and resulting foam patches, shown in Figure 4.6. Due to the higher energetics of the one-meter wave, there are three distant bubble plumes injected rather than the two in MCJ2021. After the wave plunges at the

breaking point, the wave continues propagating as a spilling wave, with splash-up, injecting air between Location 2 and 3, Location 4 and 5, and past Location 6 (approximately 14 m DFBP). The visually identified bubble plume injection locations are shown in Figure 4.7, relative to the measurement locations.

Measurement locations with short plume lifetimes τ_{plume}, Location 3 and 5 are just shoreward of the bubble plume injection locations. These locations have short τ_{plume} possibly on the account of large bubbles rising to the surface quickly and small bubbles that stay in the water column advect with the wave and away from the acoustic instruments. These smaller bubbles would stop advecting a few meters down the flume near Locations 4 and 6, resulting in longer τ_{plume} at these locations. The transducers from the acoustic velocity and attenuation system are placed in line with the width of the tank. In the x-direction of the flume, the bubble plume measurements are essentially point measurements, while foam decay and temperature time scales are calculated from cameras that have an overlapping field of view. The overlapping could smooth the spatial variability of the foam signals.

These three different locations of bubble injection suggest different stages of breaking within one wave. Previous literature[18] describes small-scale plunging waves trapping air in a vortex that is driven down by the overturning motion, creating a dense bubble plume with a high void fraction and consisting mainly of large bubbles. Also, splash-up forms an air cavity, creating a secondary bubble plume downstream of the first bubble plume. These two bubble plumes are observed by MCJ2021. However, speculation[18] states the initial splash-up did not create a secondary splash-up and resulting in a third bubble plume due to the limitations of the depth-limited conditions. Since our system is not depth-limited, there is a possibility that higher energetics created a secondary splash-up resulting in another area of high void fraction, forming the third bubble injection location onshore of Location 6.

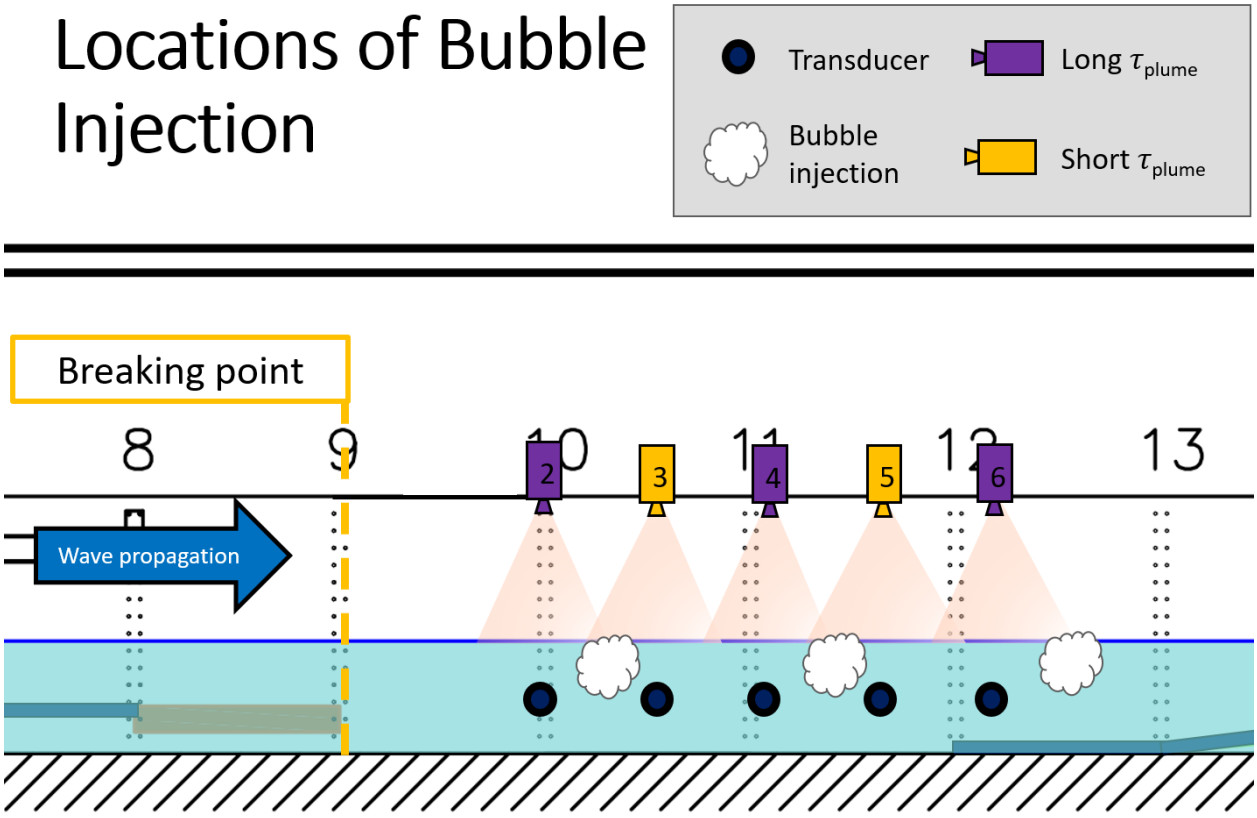

Figure 4.7: A schematic of the bubble plume injection locations relative to the measurement locations. Using the side view of the Large Wave Flume, six measurement locations were located between the breaking point and the beach. Each measurement location is symbolized with a camera icon. The overlapping field of views from the camera is represented with translucent orange triangles. Location 1 is not shown because little to no bubbles and foam were detected, and the data from Location 1 was not used in the time scale comparisons. Locations 2, 4, and 6 are purple to show these locations have long τ_{plume}. Locations 3 and 5 are yellow to show these locations have short τ_{plume}. From each location, there are circles in the water column to represent the acoustic velocity and attenuation system. Bubble injection locations are between Location 2 and 3, between Location 4 and 5, and shoreward of Location 6.

4.4 Mitigating Factors

4.4.1 Bubble Size Distribution

Large bubbles (on the order of a millimeter) have high rise velocities (i.e., > 10 cm/s) and account for a significant portion of the void fraction from air entertainment and, therefore, contribute to the surface foam generation. Smaller bubbles have a slower rise velocity and linger in the water column for longer times, and have negligible contribution to the surface foam. From bubble size distribution, bubble rise velocity, and turbulence we can infer the energy dissipated[19]. Initial bubble entertainment is broken up by turbulence, dissolution, and buoyancy, affecting the bubble size distribution. In addition to bubble size, bubble depth is an indicator of high energy stages of breaking as it takes more work to drive entrained air down into the water column[18].

4.4.2 Role of Ambient Heat Flux

The FoamEx experiment took place during the summer in Corvallis, Oregon. During this time of year, the weather is hot and relatively dry [43]. Atmospheric temperature during the week ranges from 9 to 36 $^{\circ}C$. The high and low temperatures during the duration of the measurements are shown in Table 3.1. Typically, the ocean receives inward solar shortwave radiation, net longwave radiation emitted outward from the ocean surface and reflected, outward latent heat flux of vaporization, and outward sensible heat flux from the air-sea temperature difference. In our system, there is no shortwave solar radiation since the flume is indoors. Considering it was warm indoors, there is most likely net inward long-wave radiation. The indoor nature of the facility may have created a greenhouse effect, insulating the heat loss from the tank. There is little latent heat flux due to the high saturation right above the water surface and no wind inside the facility. There is an inward sensible heat flux due to a higher air temperature than water temperature. In our system, sensible heat likely dominates the ambient total heat flux.

We examined the effect of ambient heat flux on the skin temperature difference ($\Delta T_{skin} =$

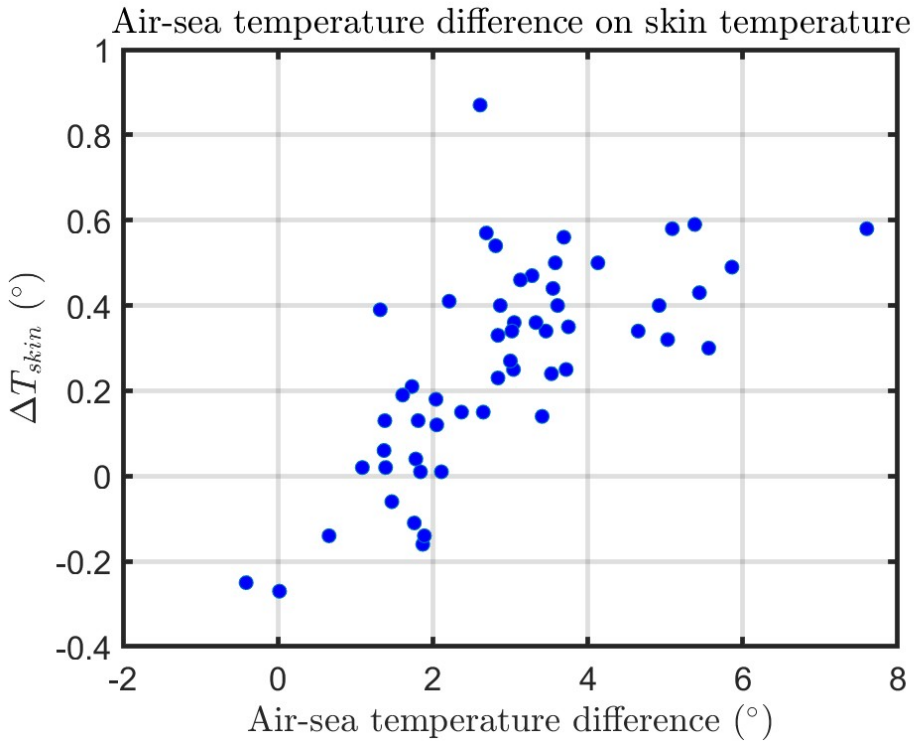

Figure 4.8: Skin temperature difference ΔT_{skin} versus air-sea temperature Difference. Each blue symbol represents each experimental run in FoamEx.

$T_{skin} - T_{sub-surface}$). Sub-surface water temperature is taken as the temperature from 5 cm below the surface, and skin temperature is from the radiometer. Representative of the ambient heat flux, we use air-sea temperature difference ($T_{air} - T_{water}$). Skin temperature difference ΔT_{skin} is linearly related to air-sea temperature difference, shown in Figure 4.8. As water temperature at different depths stays relatively constant, air temperature is the mitigating factor in ΔT_{skin}. Skin temperature is physically at the interface of air and water. As the air temperature increases, ambient heat flux increases, and increases the ΔT_{skin}.

When looking at the role of ambient heat flux on the foam temperature temperature, we examined air-sea temperature difference ($T_{air} - T_{water}$) effects on the temperature time scale t_{warm}. Air-sea temperature difference did not correlate with the temperature time scale t_{warm}, shown in Figure 4.9. This indicates that the onset of warming is not strongly affected

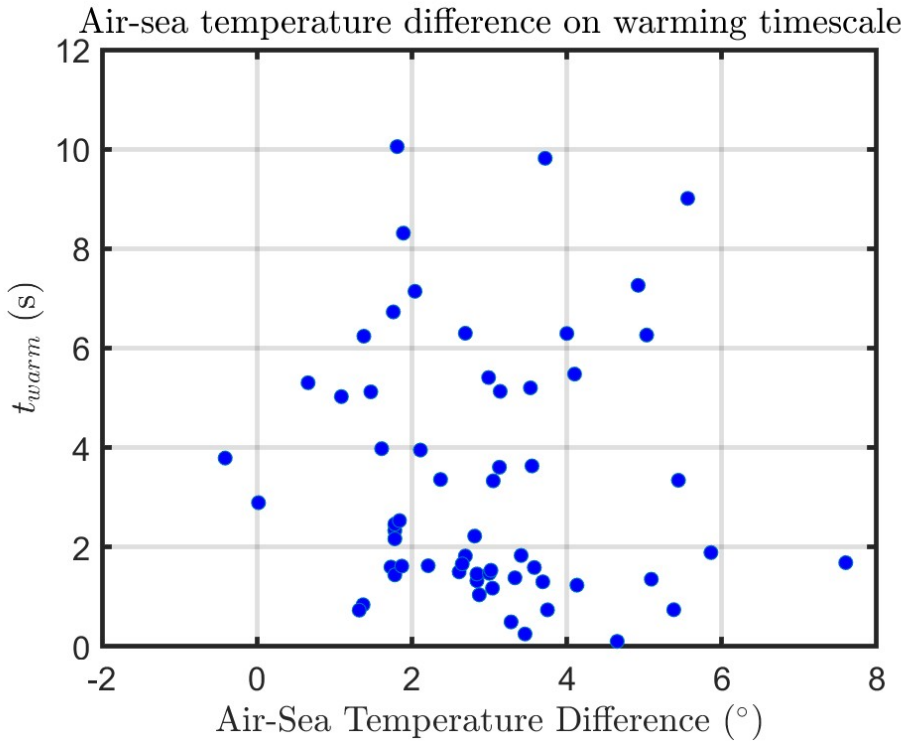

Figure 4.9: Onset of Warming Time scale t_{warm} versus Air-Sea Temperature Difference. Each blue symbol represents each experimental run in FoamEx.

by the air-water heat flux, similar to MCJ2021 where t_{cool} was not affected by environmental factors.

4.4.3 Horizontal Advection

The previous work from MCJ2021 and Callaghan (2013) study foam decay in small-scale laboratory experiments. Their small-scale experiments examined a whole wave, on aggregate. In the FoamEx experiment, split sections of a wave were observed at fixed locations along a flume. One of the scientific motivations is to compare sections or different stages within a breaking wave against an aggregate wave. MCJ2021 explored the idea of tracking individual plumes from a breaking wave, observing the deformation of bubble plumes from the turbulence and mixing from the energy of the wave and the advection from wave orbital

motion. The upward or downward force acting upon a bubble is dependent on the phase of the wave. The fluid motion causes the bubbles to move horizontally along the flume [28], affecting the geometry and location of the bubble plume, resulting in foam that is not necessarily located vertically above the bubble plume. In our experiment, the measurement locations are fixed for the duration of a run, and bubble plume decay is highly spatially variable. Measurements, particularly the in-situ observations, need to have higher spatial resolution to develop a clearer understanding of individual bubble plume dynamics.

4.4.4 Flume Limitations

Callaghan et al. (2013) addressed the limitations of conducting wave-breaking observations in a flume. In a small-scale flume, wave breaking is limited to the two-dimensional nature of a mechanical wave maker; however, in nature, wave breaking is a three-dimensional process. Flume width can constrict the lateral spreading of the breaking crest and resulting foam coverage. In addition, there could be the possibility of a limitation with the depth of the flume, restricting the injection depth of bubbles. With a 2 m water depth and assuming bubble injection is instantaneous, large bubbles with a rise velocity of 15 cm/s [45] would take bubbles approximately 13 s to rise to the surface from the bottom of the flume. Our bubble decay time scales are less than 10 s. Therefore, we assume flume depth does not impose a limitation in the FoamEx experiment.

4.5 Future Work

Factors such as bubble size distribution, the role of ambient heat flux, horizontal advection, and flume limitations conceivably affect the results significantly. Additional work is necessary to investigate the effects of these factors on the results or to prevent limitations. Further investigation on the integration of the bubble size distribution from the bubble camera and bubble depth from the acoustic velocity attenuation system into the results is necessary better to characterize the spatiotemporal evolution of the bubble plumes. ADV measurements were collected, but have not yet been explored, to infer the effects of advection and turbulence on

bubble plumes and resulting foam formation.

Adequate investigation of the time scales and spatial variability of foam and bubble decay and how they relate to energy dissipation of different stages of breaking will require tracking of the bubble plumes and foam evolution which will require high spatial resolution between measurements.

Chapter 5

CONCLUSION

This work is an extension of work done in a small-scale laboratory experiment looking at the thermal signature of residual foam left behind by breaking waves. Previous work established a correlation between the time scales of cooling foam to bubble plume lifetime and plume depth. These factors are not affected by the environmental conditions such as environmental conditions. A unique dataset of measurements taken of a field-scale laboratory experiment to look at the foam and bubble generation from breaking waves. Surfactant was added to freshwater to mimic the saltwater foam properties. The extended work used one-meter solitary waves and initiated depth-limited breaking. Measurements were collected in six different locations between the breaking point and a beach, spanning 12 m. Temperature measurements were collected at different vertical depths with temperature probes, and a radiometer measured the skin temperature of the water surface. Foam coverage area and relative foam temperature were quantified through imagery from visual and thermal infrared cameras. Bubble plume characteristics were measured by an acoustic velocity and attenuation system and an in-situ bubble camera. Wave height was measured with wire waves gauges, mounted along the flume and an ultrasonic altimeter. These datasets were used to calculate the time scales of foam temperature, foam decay, and plume decay, as well as energy dissipation rates. However, the large wave flume used in this experiment was indoors, and had a higher air temperature than water temperature, resulting in a warming foam, opposite to the cooling foam that is typical.

Though there was a warming foam, the warming temperature time scale trends are similar to the cooling foam time scales, confirming the environmental conditions do not strongly affect these time scales. There is a positive correlation between the foam decay time scales

and the warming temperature time scales. However, the data has scattered in agreement with previous work. Strong spatial variability in bubble plume lifetimes suggests different stages of wave energetics for the bubble plumes and resulting foam. The transducers have a high sensitivity to spatial variability due to their smaller spatial range; therefore, the bubble plume and resulting foam time scales are dependent on the location of bubble injection relative to the instrumentation. Further investigation is necessary in lateral plume advection, plume depth, and bubble size distribution. Future work should strive to have high spatial resolution measurement to ensure adequate tracking of the bubble plume and resulting foam evolution.

BIBLIOGRAPHY

[1] S. R. Massel, *Ocean surface waves: Their physics and prediction*. World Scientific, 2005.

[2] G. B. Airy, *Tides and waves*. B. Fellowes, 1845.

[3] J. Bosboom and M. Stive, *Coastal Dynamics*. TU Delft Open, 2021.

[4] J. McCowan, "On the highest wave of permanent type," *Philosophical Magazine*, vol. 32, pp. 351–358, 1894.

[5] J. A. Knauss, *Introduction to physical oceanography*. Waveland Pr Inc, 1978.

[6] P. Sullivan and J. McWilliams, "Dynamics of winds and currents coupled to surface waves," *Annual Review of Fluid Mechanics*, vol. 42, pp. 19–42, 12 2009.

[7] N. O. for Coastal Management. url=https://coast.noaa.gov/states/fast-facts/economics-and-demographics.html. Accessed: 2024-01-15.

[8] E. Monahan and M. Lu, "Acoustically relevant bubble assemblages and their dependence on meteorological parameters," *IEEE Journal of Oceanic Engineering*, vol. 15, no. 4, pp. 340–349, 1990.

[9] G. B. Deane and M. D. Stokes, "Scale dependence of bubble creation mechanisms in breaking waves," *Nature*, vol. 418, pp. 839–844, 2002.

[10] J. M. Kleiss and W. K. Melville, "Observations of Wave Breaking Kinematics in Fetch-Limited Seas," *Journal of Physical Oceanography*, vol. 40, pp. 2575–2604, 12 2010.

[11] H. Medwin and N. D. Breitz, "Ambient and transient bubble spectral densities in quiescent seas and under spilling breakers," *Journal of Geophysical Research: Oceans*, vol. 94, no. C9, pp. 12751–12759, 1989.

[12] S. Vagle and D. Farmer, "Measurements of bubble-size distributions by acoustical backscatter," *J. Ocean. Atmos. Tech.*, vol. 9, no. 5, pp. 630–644, 1992.

[13] S. Vagle and D. Farmer, "A comparison of four methods for bubble size and void fraction measurements," *IEEE Journal of Oceanic Engineering*, vol. 23, no. 3, pp. 211–222, 1998.

[14] C. Garrett, M. Li, and D. Farmer, "The connection between bubble size spectra and energy dissipation rates in the upper ocean," *Journal of Physical Oceanography*, vol. 30, pp. 2163 – 2171, 2000.

[15] E. Terrill and W. Melville, "A broadband acoustic technique for measuring bubble size distributions: Laboratory and shallow water measurements," *J. Atmos. and Ocean. Tech.*, vol. 17, no. 2, pp. 220 – 239, 2000.

[16] E. Lewis and S. Schwartz, "Sea salt aerosol production: Mechanisms, methods, measurements, and models," *Geophys. Monogr. Ser.*, vol. 152, 01 2004.

[17] P. H. Dahl and A. T. Jessup, "On bubble clouds produced by breaking waves: An event analysis of ocean acoustic measurements," *Journal of Geophysical Research*, vol. 100, pp. 5007–5020, 1995.

[18] C. E. Blenkinsopp and J. R. Chaplin, "Void fraction measurements in breaking waves," *Proceedings of the Royal Society A: Mathematical, Physical and Engineering Sciences*, vol. 463, no. 2088, pp. 3151–3170, 2007.

[19] A. H. Callaghan, G. B. Deane, and M. D. Stokes, "Two regimes of laboratory whitecap foam decay: Bubble-plume controlled and surfactant stabilized," *Journal of Physical Oceanography*, vol. 43, no. 6, pp. 1114–1126, 2013.

[20] E. C. Monahan, D. E. Spiel, and K. L. Davidson, *A Model of Marine Aerosol Generation Via Whitecaps and Wave Disruption*, pp. 167–174. Springer, 1986.

[21] E. C. Monahan, "Fresh water whitecaps," *Journal of the Atmospheric Sciences*, vol. 26, pp. 1026–1029, 1969.

[22] A. H. Callaghan and M. White, "Automated processing of sea surface images for the determination of whitecap coverage," *Journal of Atmospheric and Oceanic Technology*, vol. 26, pp. 383–394, 2009.

[23] M. D. Anguelova and F. Webster, "Whitecap coverage from satellite measurements: A first step toward modeling the variability of oceanic whitecaps," *Journal of Geophysical Research: Oceans*, vol. 111, 3 2006.

[24] A. H. Callaghan, G. B. Deane, and M. D. Stokes, "Observed physical and environmental causes of scatter in whitecap coverage values in a fetch-limited coastal zone," *Journal of Geophysical Research: Oceans*, vol. 113, 2008.

[25] A. H. Callaghan, G. B. Deane, M. D. Stokes, and B. Ward, "Observed variation in the decay time of oceanic whitecap foam," *Journal of Geophysical Research: Oceans*, vol. 117, 9 2012.

[26] V. Bondur and E. Sharkov, "Statistical properties of whitecaps on a rough sea," *Oceanology*, vol. 22, no. 3, pp. 274–279, 1982.

[27] O. M. Phillips, "Spectral and statistical properties of the equilibrium range in wind-generated gravity waves," *Journal of Fluid Mechanics*, vol. 156, p. 505–531, 1985.

[28] N. Masnadi, C. C. Chickadel, and A. T. Jessup, "On the thermal signature of the residual foam in breaking waves," *Journal of Geophysical Research: Oceans*, vol. 126, 2021. Post doc work that is basis for masters thesiscompare clean and dirty bubbles (with surfactantsIR and visual images of bubble plumes.

[29] E. B. Kraus and J. A. Businger, *Atmosphere-Ocean Interaction*. Oxford University Press, 2 ed., 1994.

[30] E. L. Andreas, "A new sea spray generation function for wind speeds up to 32 m s^1," *Journal of Physical Oceanography*, vol. 28, pp. 2175 – 2184, 1998.

[31] S. Poulain, E. Villermaux, and L. Bourouiba, "Ageing and burst of surface bubbles," *Journal of Fluid Mechanics*, vol. 851, pp. 636 – 671, 2018.

[32] E. Andreas and E. Monahan, "The role of whitecap bubbles in air–sea heat and moisture exchange," *Journal of Physical Oceanography - J PHYS OCEANOGR*, vol. 30, pp. 433–442, 02 2000.

[33] D. Jeong, B. K. Haus, and M. A. Donelan, "Enthalpy transfer across the air–water interface in high winds including spray," *Journal of the Atmospheric Sciences*, vol. 69, pp. 2733 – 2748, 2012.

[34] C. C. Chickadel, R. Branch, W. E. Asher, and A. T. Jessup, "Laboratory heat flux estimates of seawater foam for low wind speeds," *Remote Sensing*, vol. 14, 2022.

[35] A. T. Jessup, C. J. Zappa, and H. Yeh, "Defining and quantifying microscale wave breaking with infrared imagery," *Journal of Geophysical Research: Oceans*, vol. 102, pp. 23145–23153, 10 1997.

[36] G. O. Marmorino and G. B. Smith, "Bright and dark ocean whitecaps observed in the infrared," *Geophysical Research Letters*, vol. 32, 6 2005.

[37] O. S. U. C. of Engineering. https://engineering.oregonstate.edu/wave-lab/facilities/large-wave-flume. Accessed: 2024-01-12.

[38] M. Lichti and H.-J. Bart, "Particle measurement techniques in fluid process engineering," *ChemBioEng Reviews*, vol. 5, no. 2, pp. 79–89, 2018.

[39] A. Lavery and T. Ross, "Acoustic scattering from double-diffusive microstructure," *J. Acoust. Soc. Am.*, vol. 122, no. 3, pp. 1449–1462, 2007.

[40] C. Bassett, A. Lavery, T. Maksym, and J. Wilkinson, "Laboratory measurements of high-frequency, acoustic broadband backscattering from sea ice and crude oil," *The Journal of the Acoustical Society of America*, vol. 137, no. 1, pp. EL32–EL38, 2015.

[41] E. Lamarre and W. Melville, "Instrumentation for the measurement of void-fraction in breaking waves: laboratory and field results," *IEEE Journal of Oceanic Engineering*, vol. 17, no. 2, pp. 204–215, 1992.

[42] T. M. Inc., "Matlab version: 9.13.0 (r2022b)," 2022.

[43] "Daily weather data," Jan 2022.

[44] W. H. Munk, "The solitary wave theory and its application to surf problems," *Annals of the New York Academy of Sciences*, vol. 51, no. 3, pp. 376–424, 1949.

[45] I. Leifer, R. Patro, and P. Bowyer, "A study on the temperature variation of rise velocity for large clean bubbles," *Journal of Atmospheric and Oceanic Technology - J ATMOS OCEAN TECHNOL*, vol. 17, pp. 1392–1402, 10 2000.

[46] A. H. Callaghan, M. D. Stokes, and G. B. Deane, "The effect of water temperature on air entrainment, bubble plumes, and surface foam in a laboratory breaking-wave analog," *Journal of Geophysical Research: Oceans*, vol. 119, no. 11, pp. 7463–7482, 2014.

[47] A. H. Callaghan, G. B. Deane, and M. D. Stokes, "A comparison of laboratory and field measurements of whitecap foam evolution from breaking waves," *Journal of Geophysical Research: Oceans*, vol. 129, no. 1, p. e2023JC020193, 2024. e2023JC020193 2023JC020193.

[48] J. W. Caruthers, P. A. Elmore, J. C. Novarini, and R. R. Goodman, "An iterative approach for approximating bubble distributions from attenuation measurements," *J. Acoust. Soc. Amer.*, vol. 106, pp. 185–189, 1999.

[49] D. Chu and T. Stanton, "Application of pulse compression techniques to broadband acoustic scattering by live individual zooplankton," *J. Acoust. Soc. Am.*, vol. 104, pp. 39–55, 1998.

[50] I. M. Cohen and P. K. Kundu, *Fluid mechanics*. Elsevier, 2004.

[51] B. L. Mehaute, *An Introduction to Hydrodynamics and Water Waves*. Springer-Verlag, 1976.

[52] T. Maddux, E. Cowen, D. Foster, M. Haller, and T. Stanton, "The cross-shore sediment transport experiment (crosstex)," 04 2007.

[53] H. Medwin, "In situ acoustic measurements of microbubbles at sea," *J. Geophys. Res.*, vol. 82, no. 6, pp. 971–976, 1977.

[54] H. Medwin, "Acoustical determinations of bubble-size spectra," *J. Acous. Soc. Am.*, vol. 62, no. 4, pp. 1041–1044, 1977.

[55] H. Medwin and C. Clay, *Fundamentals of Acoustics Oceanography*. Boston, MA: Academic Press, 1998.

[56] M. Miche, "Mouvements ondulatoires de la mer en prodondeur constante ou decrousante," tech. rep., École des Ponts ParisTech, Paris, 1944.

[57] E. Terrill, W. Melville, and D. Stamski, "Bubble entrainment by breaking waves and their influence on optical scattering in the upper ocean," *J. Geophys. Res. - Oceans*, vol. 106, no. C8, pp. 16815–16823, 2001.

[58] G. Turin, "An introduction to matched filters," *IRE Trans. Inf. Theory*, vol. 6, no. 3, pp. 311–329, 1960.

[59] H. Yuen, J. Princen, J. Illingworth, and J. Kittler, "Comparative study of hough transform methods for circle finding," *Image and vision computing*, vol. 8, no. 1, pp. 71–77, 1990.

Appendix A

TIME SERIES OF FOAM COVERAGE, FOAM TEMPERATURE, AND EXCESS ATTENUATION

This section holds figures of time series for foam coverage fraction, foam temperature, and excess attenuation for the different measurement locations. Each run in Figure A.1 and A.2 are shown as grey lines. The ensemble average of the measurement location is shown in red. The grey-shaded areas represent error within a standard deviation.

Notice for foam coverage fraction, at wave breaking, t = 0, foam coverage rapidly increases then rapidly decreases. The shape of the curve is different for each measurement location. Locations three and five curves have two local peaks. This could be because of the effects of surfactants[47] and the bubble plume evolution spatial variability.

Notice, in Fig. A.2, that each run has a high spread in data at one location. Generally, foam temperature rapidly decreases after wave breaking, t = 0, stays at a fixed minimum temperature for a period, and gradually increases to the initial temperature. The fixed minimum temperature is the bulk temperature below the skin layer.

These plots of excess attenuation α were processed by C. Bassett. Location One is not shown because little to no bubbles were present to show a significant change in attenuation.

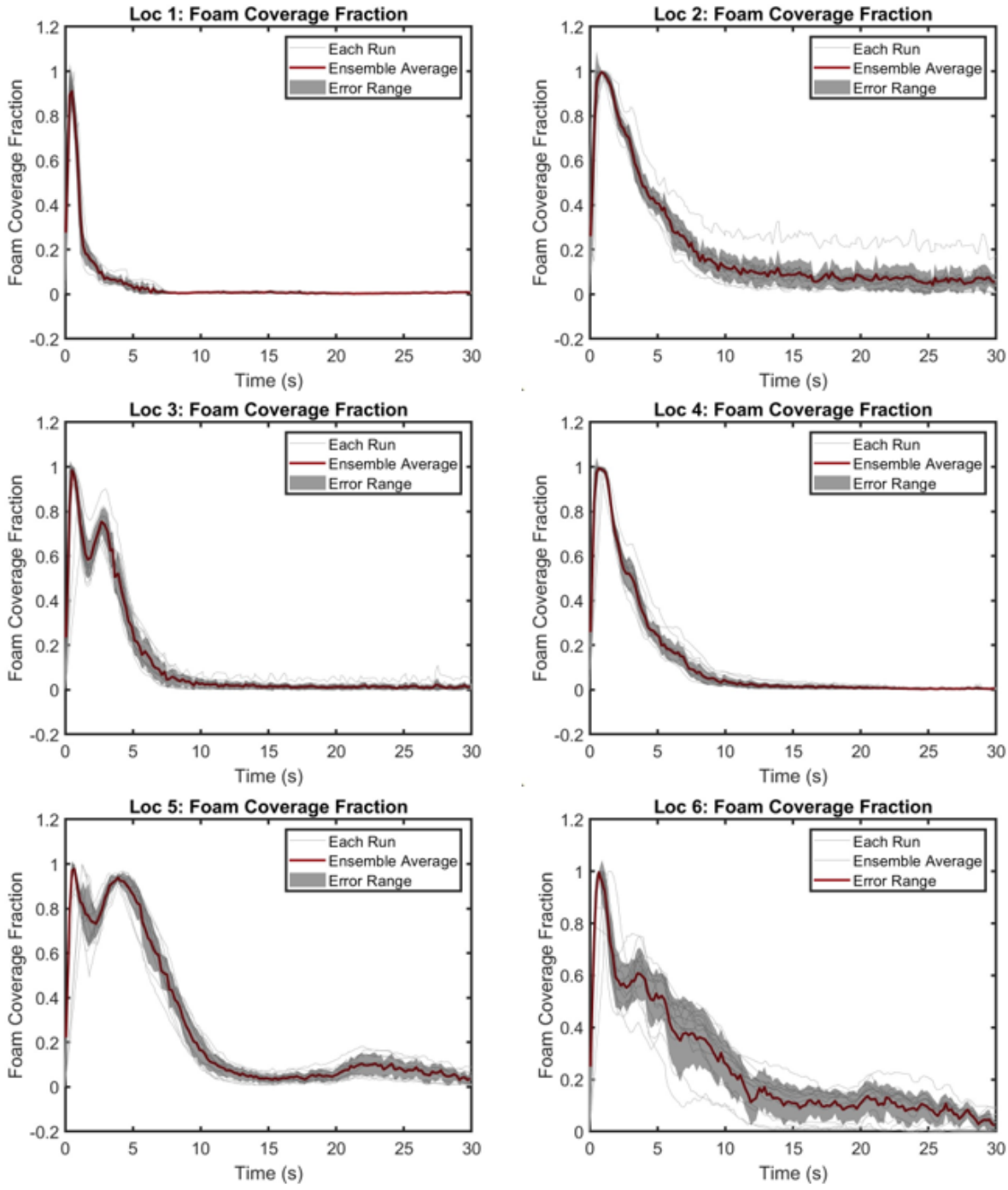

Figure A.1: Foam Coverage Fraction for Locations 1, 2, 3, 4, 5, and 6.

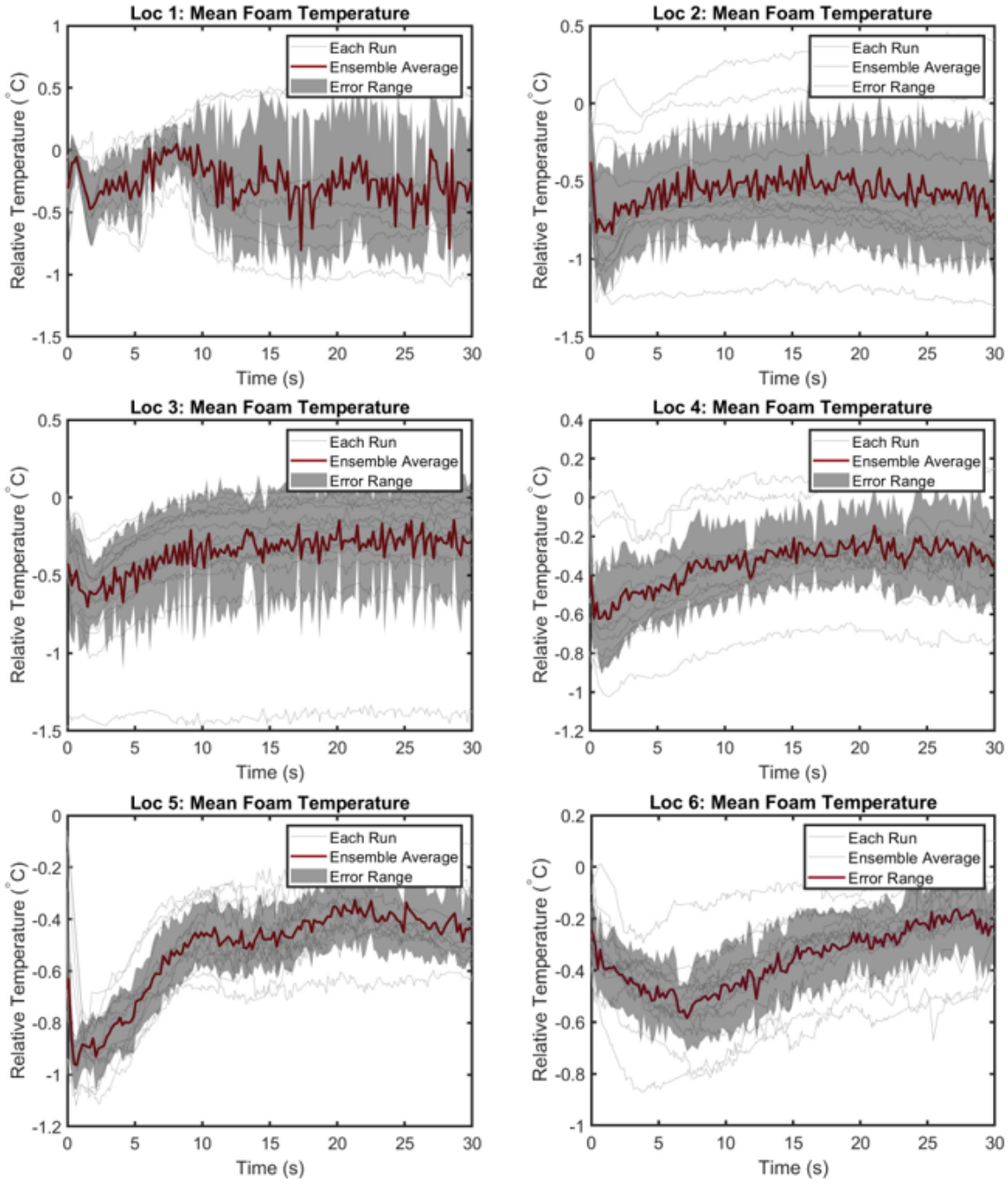

Figure A.2: Foam Temperature for Locations 1, 2, 3, 4, 5, and 6.

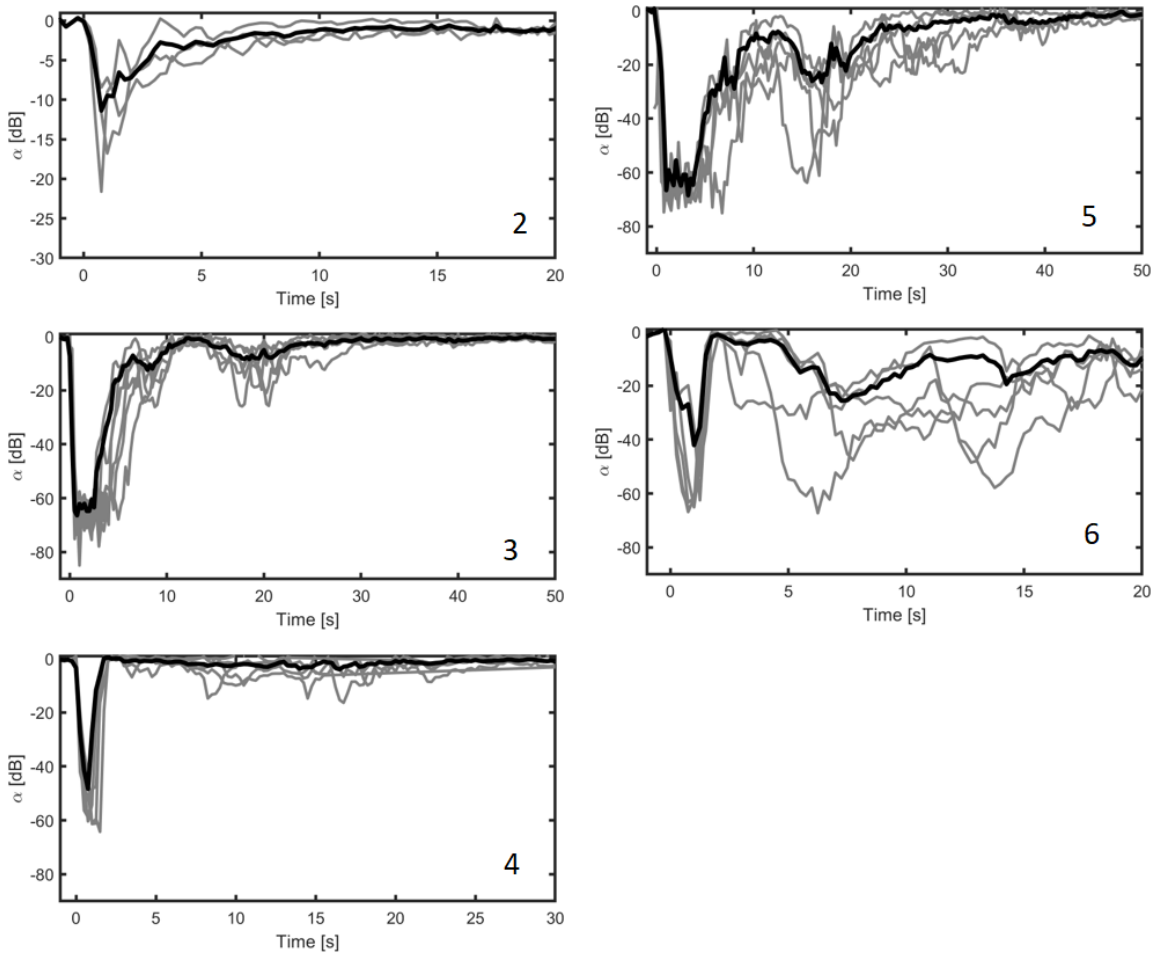

Figure A.3: Excess Attenuation for Locations 2, 3, 4, 5, and 6. These plots are associated with 7 kHz and 450 μm radius bubbles. The grey lines represent each run, and the black line is the mean excess attenuation for all the runs for that measurement location.

Appendix B

ACOUSTIC BUBBLE MEASUREMENT METHODS

This section summarizes acoustic measurements supporting the work in the main document of this document. These measurements were performed by Dr. Christopher Bassett who also drafted the text in this section.

To measure excess attenuation, we made modest modifications to a laboratory system developed by Woods Hole Oceanographic Institution and modeled after the system used by [15]. The system, which we refer to as a transmissometer, consists of two acoustic sources (ITC-1001 and ITC-1042) and two hydrophones (Teledyne/Reson TC4014-5). The sources and hydrophones were mounted on ¼" stainless steel rods extending from a frame constructed from 80-20 bars of various sizes. For experiments at Hinsdale, the full assembly was fastened to Unistrut channels on the tank's gantry/cart systems, allowing for the sensors to be easily moved with other sensors.

The ITC-1001 is a relatively low-frequency source with a resonance frequency at approximately 16.5 kHz and a strong, frequency dependent transmit voltage response (TVR). We refer to this as the low-frequency source. In contrast, the ITC-1042 also exhibits a strong TVR but has a resonance frequency at 79 kHz. These transducers were installed on the ends of the frame with the hydrophones placed between them. The distance between the sources and receivers were measured manually but, also, determined acoustically in fresh water. This was done by transmitting the signals used in the experiment and cross-correlating the received signals from the hydrophones with the transmit signal (see Sec. B.0.2 for additional details). Using the sound speed measured using a Sontek Castaway CTD, the distances between the sources and hydrophones were 0.24 m (low-frequency) and 0.27 m (high-frequency).

.

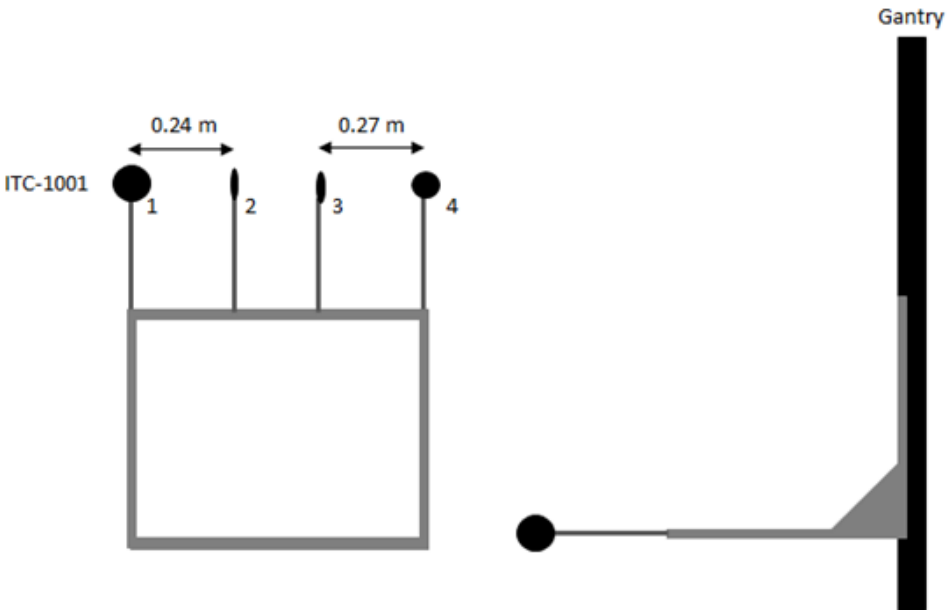

Figure B.1: (1) The low-frequency source (ITC-1001), (2) hydrophone for low-frequency measurements, (3) hydrophone for high-frequency measurements, and (4) the high-frequency source (ITC-1042)

B.0.1 Control and data acquisition

The transmissometer controlled and acquired data using a personal computer (PC) and custom software written in MATLAB (Fig. B.2). The PC was connected to a National Instruments USB-6366 board via a USB cable. Two output channels from the board were connected to a dual-channel power amplifier powered by a 12 VDC power supply. Each output from the power amplifier was connected to one of the acoustic sources. Additional circuity to provide 120 VAC power to a 12 VDC power supply, which powered the power amplified and hydrophones. The two hydrophones, also connected to the 12 VDC power supply, were connected via BNC cables to Thorlabs EF111 1 kHz high pass filters. These high-pass filters were installed to suppress the hydrostatic pressure fluctuations associated with waves in the tank. The outputs from the high pass filters were then connected via USB back to two input channels on the USB-6366 board.

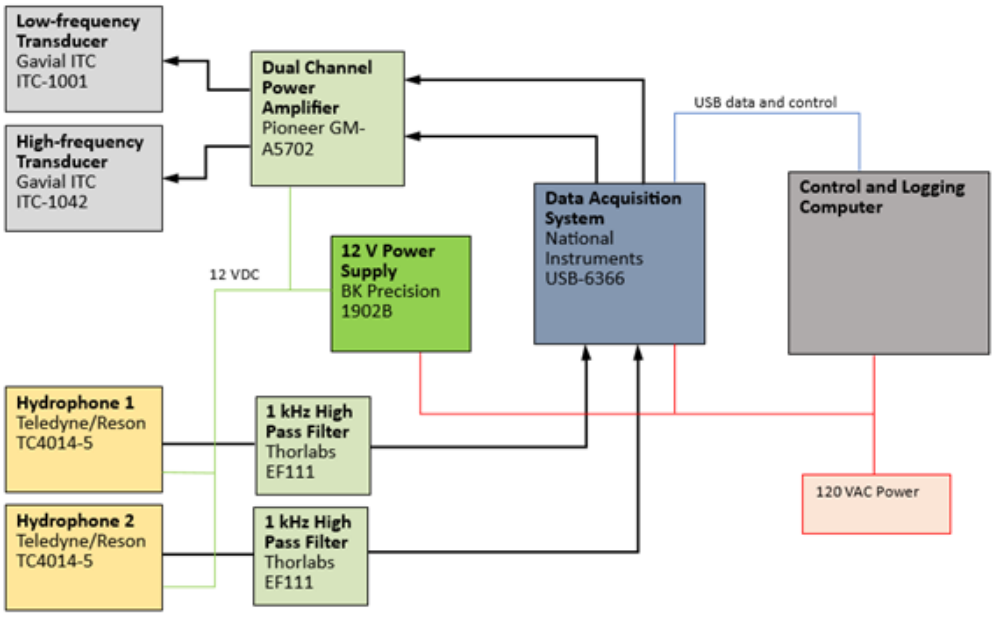

Figure B.2: A box diagram showing the components of the transmissometer.

To operate the system the custom MATLAB script was programmed to transmit a signal every 0.125 s during operations, switching between the low- and high-frequency channels to generate two independent time series with 0.25 s resolution. The low-frequency transducer transmitted a 1 μs frequency modulated chirp from 4-28 kHz. High-frequency transmit signals had the same duration with a bandwidth from 30-100 kHz. Because both of the transducers have strong frequency responses, the signal amplitude of a linear chirp was modified by the inverse of the TVR and scaled to have peak values less than +/- 1 V (the maximum output of the board). Transmit signals were created with a sampling frequency of 1 MHz and the hydrophone recorded data at 1 MHz but were downsampled to 250 kHz, prior to saving the data. The total number of transmit pings was occasionally modified in the script, thereby changing the duration of saved files. In most cases, the system was confirmed to transmit 240 pings on each transducer, which corresponds to four minutes of sampling. At the close of each file, the software had to write data from the buffer and close the file, resulting in system downtime. To the greatest extent possible, the system acquired

15 s of data prior to the beginning of each breaking wave event with two or three total files recorded, representing 8-12 minutes.

To verify system operations a series of dockside tests were performed prior to the experiments at OSU. The goal of these dockside tests was rescale the amplitude to maximize the power without saturating the receivers and to generate "replica" signals to use in matched filter (or pulse compression) processing [58, 49] of experimental data. Examples of these outputs for both hydrophones are shown in Figure B.3. The top rows show the transmitted voltages and the middle rows show the received, downsampled signals. These show the transmitted signals had relatively constant amplitudes across the bandwidth despite the frequency dependence of the transducers TVRs.

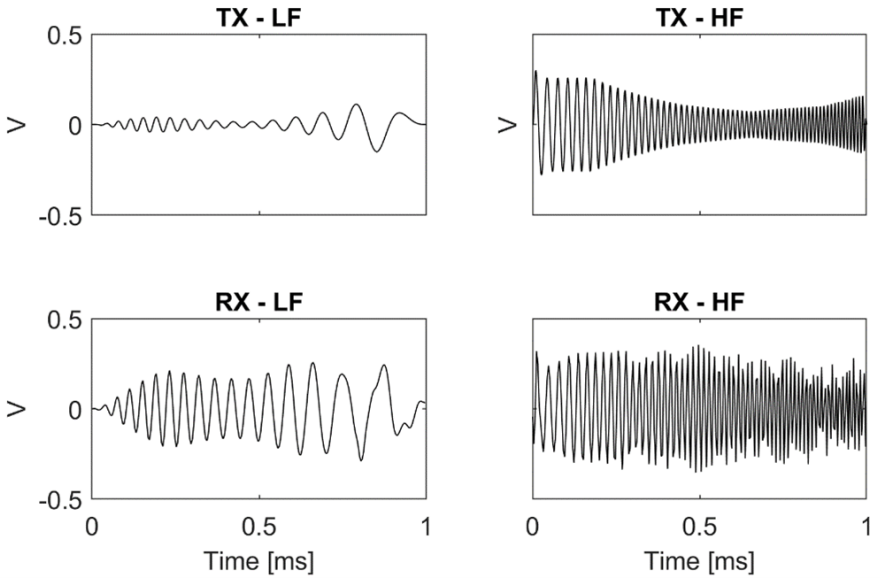

Figure B.3: (top) Transmit (voltage) time series for the low- (LF) and high-frequency (HF) transducers. (bottom) Received signals recorded by the hydrophones. The received signals show the amplitudes were relatively constant across the transmitted bandwidth and that significantly increasing the transmit power would have saturated the data acquisition board (+/- 1 V). These signals were used as replicas for pulse compression operations with the experimental data (Sec. B.0.2).

B.0.2 Transmissometer processing

Each recorded file constrained a time vector, two time series representing the low- and high-frequency hydrophones, and metadata. In practice, both the hydrophones recorded signals from both the low- and high-frequency transducers, but high attenuation rates during breaking events over the longer path length made it easier to only work with the hydrophone closer to a given transmitter. The received data array was broken into independent time series for the two hydrophones, then restructured into arrays containing each ping. To identify the arrival time of the ping in each window, the relevant replica signals were cross-correlated with the received signal. This process was particularly important because of the relative proximity to the surface. More specifically, the direct path length for the low-frequency transducer was 24 cm while the surface bounce path was approximately 60 cm. Because the transmit signal was 1 ms in duration, the pulse length was approximately 1 m and these signals overlap temporally. However, since the range resolution of pulse compressed signals is approximately $c/2B$, where B is the transmitted bandwidth the range resolutions of the transmitted signals with sound speeds of approximately 1500 m/s both on the order of 4 cm or less. The distinct arrivals are, therefore, easily separable.

Next, the peaks in the pulse compressed signals are identified over the period corresponding to arrival, accounting for the potential for significant decreases in sound speed due to relatively high gas volumes in the water. Once the peak is identified a 2 ms window beginning when with the transmission of the signal, a Fast Fourier Transform of 100 data points centered on the peak, zero padded to 214 points, is used to calculate the power spectrum. The same process is repeated for all pings. To calculate the attenuation, a "calibration" spectrum is determined by taking the median of the first 10 pings in the dataset. These values are chosen to correspond to periods when the tank is quiescent. Finally, the total attenuation as a function of frequency is determined by subtracting the log transformed (i.e., $10\log_{10}$) power spectrum data for each ping from the calibration values. An example of this process from received ping through α for one ping under quiescent conditions and another following

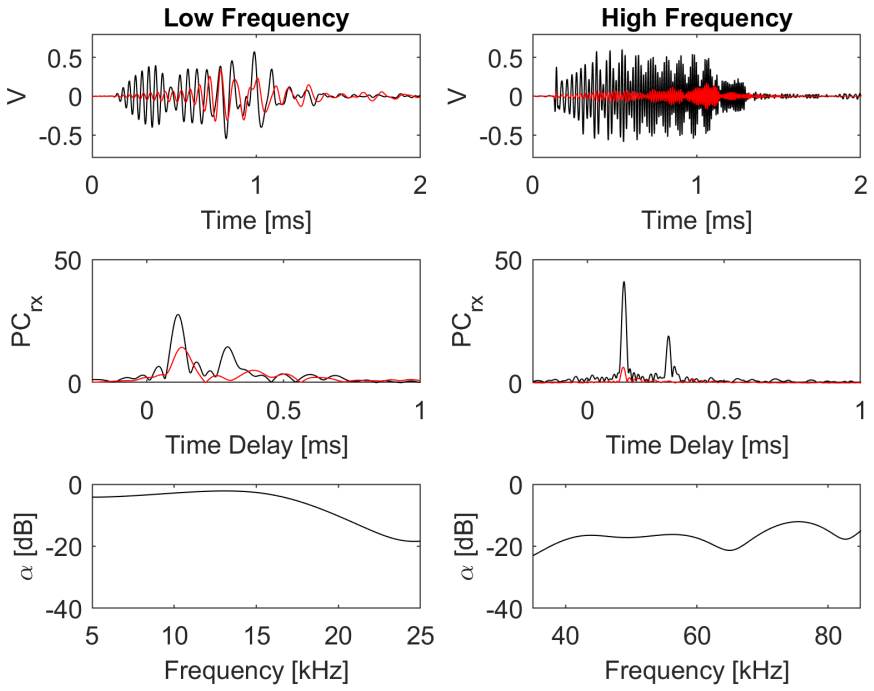

Figure B.4: (Top row) Received signals under quiescent conditions (black) and following after a breaking wave (red). (Middle row) Pulse compressed signals corresponding to the received data in the top row. (Bottom row) Attenuation curves correspond to the period following the breaking wave (the black signals in the top two rows are an example of a "calibration" ping).

a breaking wave is shown in Figure B.4 for both the low- and high-frequency transducers.

An example time series of α curves is shown during a breaking wave event in Figure B.5. In these observations, both the low- and high-frequency signals are attenuated to the noise floor of the system, immediately after the breaking event. After a couple of seconds, the signal starts to return with signal levels within 10 dB of the pre-breaking values after approximately 8 s at the low frequencies. In contrast, relatively high levels of attenuation are observed throughout the 45 s period after breaking for the high-frequency transducers.

Two data products are used to analyze the bubbles from the experiment. The first is simply the measured attenuation. The second is estimates of void fraction. The response

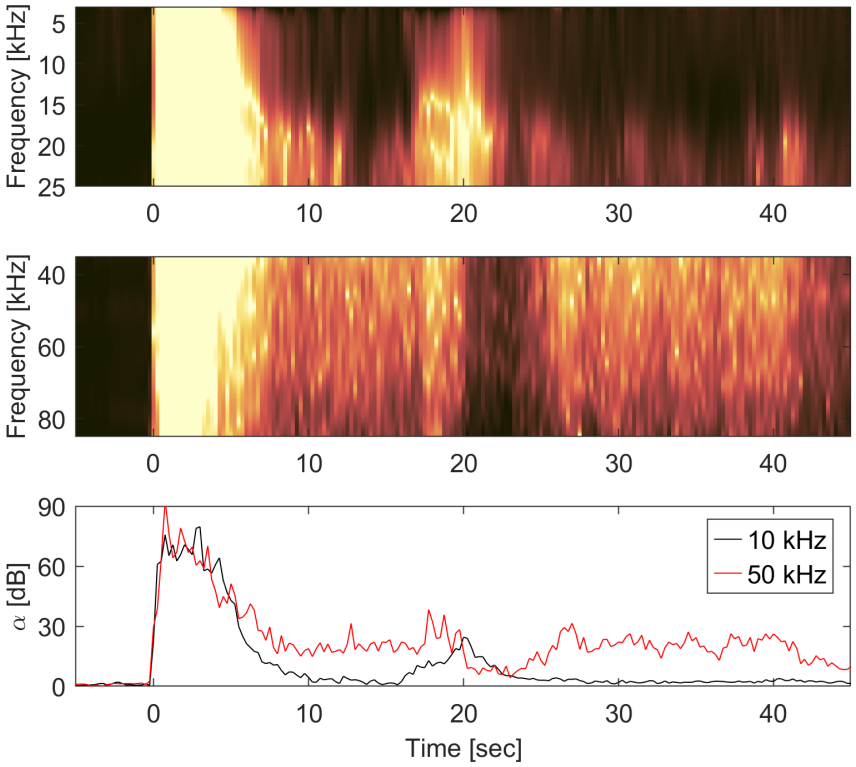

Figure B.5: Example data from a wave breaking event. (Top) Attenuation in the low-frequency channel. (Middle) Attenuation in the high-frequency channel. (Bottom) Time series of attenuation at two frequencies. Note that relatively high levels of attenuation at high-frequencies persist for much longer than at low-frequencies.

of bubbles present in the water column to acoustic signals is typically modeled as harmonic oscillators. Due to the large differences between the acoustic properties (sound speed and density) of water and air, bubbles can scatter significant amounts of sound. Scattering, when coupled with absorption, results in acoustic extinction (or attenuation) of signals. Like other harmonic oscillators, scattering or extinction curves for bubbles exhibit a frequency dependence. Near the surface, bubbles have a strong resonance peak near $ka = 0.0136$, where k is the acoustic wavenumber and a is the radius of the bubble. In practice, the resonance frequency of a bubble is dependent on environmental conditions and material properties. Nonetheless, for a spherical bubble in water, the resonance frequency f_r can be approximated as

$$f_r = \frac{3.25\sqrt{1 + 0.1d}}{a}, \tag{B.1}$$

where a is the radius of a bubble in meters and d is the depth. [55]

Numerous references have explored the use of excess attenuation due to bubbles to estimate bubble size distributions. Through a series of simplifying assumptions, the complex theoretical relationships between extinction and bubble size distribution can be simplified to a simple expression:

$$n(a) \approx \frac{4.6e - 6f^3\beta(f)}{1 + 0.1d}, \tag{B.2}$$

Where $n(a)$ is the bubble size distribution, f is the resonance frequency for bubbles with radius a, β is the measured excess attenuation in dB/m, and d is the depth [48]. For near-surface measurements, the denominator can be neglected further simplifying the relationship. This formulation is referred to as the resonant bubble approximation because it assumes that contributions to measured excess attenuation are driven solely by bubbles that are resonant at a given frequency. A limitation of this approach is it assumes bubble size distributions follow a power law. Implying numerical densities of larger bubbles are much smaller than those of smaller bubbles; otherwise, the off-resonance contribution of large bubbles will bias the results [54]. Fortunately, such power laws have been shown to be widely observed for bubbles resulting from breaking waves, using a variety of techniques [53, 54, 12, 13, 9, 15, 57].

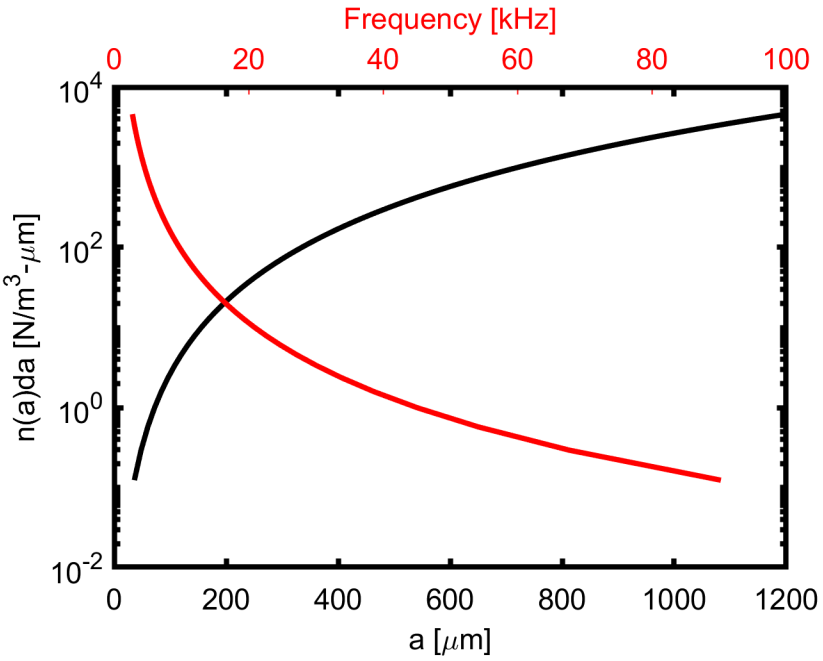

Figure B.6: Modeled bubble size distributions assume $\beta(f) = 1$ dB. Bubble radii and associated frequencies are shown on x-axes.

As a result, Eq. B.1 provides a simple formulation for estimates of bubble size density over a range of frequencies, using measurements of attenuation.

Equations B.1 and B.2 show that (1) the resonance frequency is inversely proportional to the bubble radius; while for a given level of excess attenuation, the number of bubbles present scales with f^3. Fig. B.6 shows bubble size distributions from the resonant bubble approximations assuming $\beta = 1$ dB/m for frequencies from 3 to 90 kHz, which corresponds to bubble radii from approximately 37 μm to greater than 1 mm. This shows for that small bubbles must be present in considerably high numbers at high frequencies to result in similar levels of attenuation of relatively small numbers of bubbles at low-frequencies.

Because excess attenuation due to bubbles can be easily related to their numerical density, and therefore, the volume of gas, direct measurements of α, or the total observed attenuation across the path length as a function of time are a relatively simple approach to visualizing

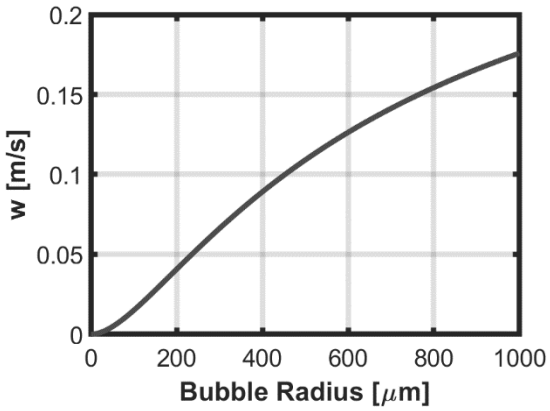

Figure B.7: Rise velocities for “dirty" bubbles[16].

the presence of and time scales associated with bubbles of specific sizes. Here, the focus is on relatively large bubbles (i.e., a >100s of μm due to the relationship between a bubble's size and its rise velocity, which brings the bubbles back to the surface after a wave breaks. Bubble rise velocities can be estimated by $w = \frac{33a^2}{(a+0.37)^2}$, where a is the bubble radius in mm and w is the rise velocity in cm/s [16]. Figure B.7 shows that small bubbles (e.g., a <100 μm) have rise velocities of only a couple of cm/s or less. Thus, if they are injected to depths of a half meter or greater, they will have long residence times. In contrast, larger bubbles may have rise velocities exceeding 10 cm/s.

To obtain an estimate of the void fraction $n(a)da$ is integrated over all or a relevant portion of the curve with scalar factors to account for the volume of a bubble. Here, this integration is performed over a limited portion of $n(a)da$ where bubbles are relatively large and would naturally rise with speeds on the order of 10 cm/s or greater. This corresponds to radii of approximately 400 μm. Estimates of plume time scales are calculated by taking the time series of the integrated void fraction and identifying the total time from the initiation of breaking until the void fraction signal has returned to 37% of its peak value. While the void fraction signal does “saturate" due to the loss of the signal in extreme cases, this time scale still provides a reasonable and consistent approach to calculating the time period for most

of the bubbles over the relevant size range to rise about the instruments. Note in addition that the total time for bubbles to rise to the surface is not measured by the transmissometer, which was approximately 22 cm below the surface. Thus, an offset of 1.5 s is the void fraction time scale to account for the time for the bubbles to rise back to the surface.

Appendix C

BUBBLE IMAGE PROCESSING

This section summarizes Bubble Image Processing supporting the work in the main document of this document. Preliminary data processing was conducted by Dennise Aguilar Cano, and Dr. C. Christopher Chickadel drafted the text in this section.

The bubble camera system was located 25 cm below the surface of the still water level at the onshore edge of the IR and EO camera fields of view, and the system is described previously in the Methods section. The system is designed to image bubbles through the shadowgraph technique based on [38] and relies on columnated backlighting and a telecentric lens to produce an image with negligible perspective distortion. As shown in Figure C.1, bubbles appear dark since their curved surfaces refract the incident light away from the view camera. The bubbles within the in-focus portion of the depth of field have sharp edges, while bubbles that are too close or too far away appear increasingly blurred, depending on their distance from the in-focus region. To identify and measure bubbles and their sizes, we used the MATLAB (2022) function `imfindcircles`, which in turn uses the Circular Hough Transform [59] to detect and measure circular features. We tested and adjusted the parameters to this algorithm to maximize agreement with a small set of manually processed bubble images. The detection parameters were intentionally limited to find bubbles that were in focus between 5 - 100 pixels, or 0.075 - 1.5 mm, radius for our camera system setup.

Figure C.1 shows an example of a cropped, raw bubble image from the experiment. Before being input to `imfindcircles` the raw images were normalized by a base image taken in the time before the wave was initiated when bubbles were not present. The normalized image was thresholded with a constant percentile, image histogram-based value and cleaned to fill holes and remove stray pixels. The processes produced binary image of bubbles (1)

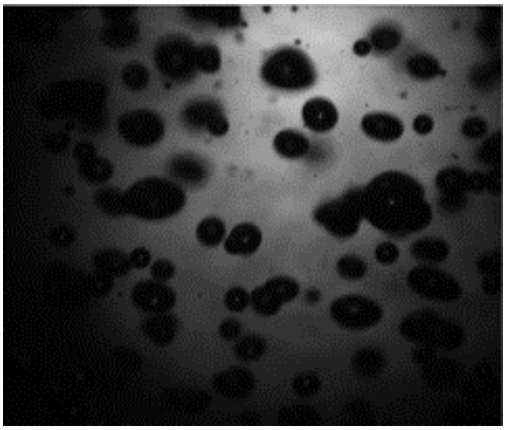

Figure C.1: A single frame is taken from the submersible camera and light system. There is vignetting around the image due to light being partially blocked. With the shadowgraph technique, the bubbles present as black shadows.

and background (0), which was then subject to `imfindcircles`. An example of the bubbles identified from the raw image example in Figure C.1 using is shown in Figure C.2, and it's noteworthy that the algorithm can attempt and generally succeed in detection of bubbles that are overlapping in the two-dimensional image. This method was repeated on each image frame for each wave run (approximately 10 Hz imagery over 3-5 minutes, over 1000 frames per run) to derive time series of bubble number and radius. Runs from the same location were combined through an ensemble histogram, using the time the wave entered into the plan-view image view as $t = 0$ and time bins of 0.2 s (see Figure 3.7).

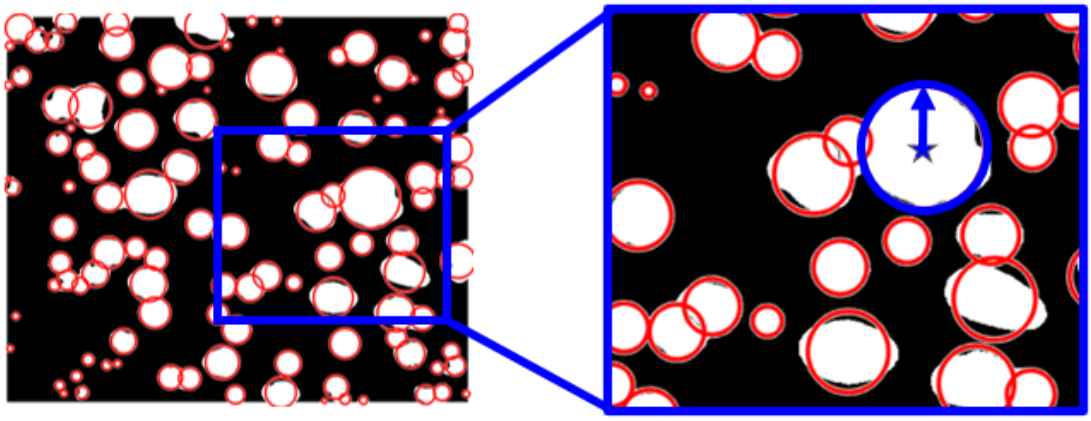

Figure C.2: The image on the left is the processed image from Figure C.1. The image was binarized to separate bubbles from the background. The approximate bubble location and size are shown with red outlines of the bubbles' circumference. The image on the right is an expanded view from the blue box. The highlighted bubble (blue star) shows the measure of the center to the circumference to find the radius.